https://doi.org/10.5194/egusphere-2026-6696
Preprint. Discussion started: 4 November 2026
© Author(s) 2026. CC BY 4.0 License.

Morphological Classification of the Lower Stratospheric Polar Vortex Edge as a Finite-Width Potential Vorticity Band

Yonatan Givon[1], Joanna Wesniuk[1], Robert C. J. Wills[1]

[1]Institute of Atmosphere and Climate, ETH Zurich, Zurich, Switzerland

Correspondence to: Yonatan Givon (Yonatan.givon@env.ethz.ch)

Abstract. The stratospheric polar vortex (SPV) is a dominant feature of the winter stratosphere, characterized by circumpolar westerly winds. Its lowermost edge is a key region of troposphere–stratosphere coupling. Shaped by Rossby wave breaking (RWB), the morphology of the lower-SPV edge reflects changes in jet-stream orientation, storm-track activity, and atmospheric blocking, and is linked to surface weather and the upward propagation of wave activity. The nonlinear potential-vorticity (PV) dynamics in this region motivate approaches that capture its evolving structure. However, existing classifications typically represent the SPV edge as a pointwise boundary, overlooking the gradual transition between the stratosphere troposphere suggested by tracer observations. Here, we treat the lower-SPV edge as a finite-width boundary region whose width and morphology define distinct circulation regimes.

We develop a daily, year-round classification based on recurring configurations of a lower-stratospheric PV band, defined by the area between two PV contours. We focus on the 6–7 PVU band on the 350-K isentropic surface, which remains in the stratosphere year-round, closely follows the maximum PV gradient and subpolar jet, and provides a measure of jet intensity through its width. A self-organizing map (SOM) identifies 12 regimes.

These regimes span configurations associated with regional blocking and hemispheric annular modes, including variations in SPV core strength and edge sharpness. Each regime exhibit distinct lower-stratospheric PV anomalies, surface temperature and pressure patterns, and tropospheric heat, momentum, and transient-wave activity fluxes. Transition and persistence statistics reveal preferred pathways toward SPV weakening, with Scandinavian, North Pacific, and Greenland blocking emerging as prominent precursors of negative PV anomalies in the lower-SPV core. Changes in 10-hPa wind speed across regime transitions further reveal systematic SPV preconditioning and responses. Finally, anomalous regime occupancies before and after sudden stratospheric warmings (SSWs) highlight the potential of this framework for understanding and predicting SSW events.

https://doi.org/10.5194/egusphere-2026-6696
Preprint. Discussion started: 4 November 2026
© Author(s) 2026. CC BY 4.0 License.

1. Introduction

The stratospheric polar vortex (SPV) is a coherent, large-scale flow structure consisting of persistent circumpolar westerly winds (Butchart and Remsberg, 1986; Waugh et al., 2017). It encompasses the lower- to upper-stratosphere from the pole to the subtropics, intensifying during wintertime in each hemisphere and decaying as summer approaches (Schoeberl et al., 1991; Zuev and Savelieva, 2024). On synoptic-to-subseasonal timescales, the winter SPV is known for its substantial spatial-temporal variability, as evident in the morphological configuration of the SPV edge (McIntyre 1982; McIntyre and Palmer, 1993; Mitchell et al., 2011). The morphological structure of the SPV edge has been associated with the occurrence of various tropospheric weather patterns, as equatorward SPV displacements are associated with troughing, cyclogenesis, and cold anomalies, and vice versa for poleward SPV displacements (Haynes et al., 1991; Kolstad et al., 2010; Lee et al., 2019; Zuev et al., 2022; Afargan-Gerstman and Domeisen, 2025).

The lowermost SPV edge (also termed the tropospheric polar vortex edge or dynamical tropopause, Waugh et al., 2017) denotes the dynamical boundary between tropospheric and stratospheric air masses, forming a dynamical transport barrier and limiting the vertical propagation of tropospheric Rossby waves. Specifically, Charney and Drazin (1961) showed that stationary planetary waves can propagate vertically only within a range of background westerly winds, with sufficiently strong westerlies inhibiting upward propagation. More generally, the vertical propagation of Rossby-wave activity depends on the three-dimensional background flow and its refractive properties. Easterlies and intense zonal winds are shown to supress Rossby wave interaction with the SPV core (Nash et al., 1996; Mizuta and Yoden, 2001; Rypina et al., 2007), while relatively weak westerlies promote it. The dynamical barrier associated with the lowermost SPV edge morphology therefore affects the likelihood of tropospheric perturbations to penetrate the stratosphere.

The prevailing westerly flow of the lower-SPV is frequently perturbed regionally and temporally under torques imposed primarily by Rossby wave breaking (RWB) events (Baldwin and Holton, 1988; Matrius et al., 2009; Garfinkel et al., 2010). RWB events involve the overturning of potential vorticity (PV) contours along the lower-SPV edge (Barnes and Hartmann, 2012). This overturning significantly deforms the SPV edge, producing elongated filaments of lower (higher) PV that penetrate poleward (equatorward). These perturbations displace the SPV edge and thus the orientation of storm tracks (Kidston et al., 2015) and can propagate upwards to interact with the SPV core. RWB events are therefore considered a major component of SPV spatio-temporal variance (Garfinkel and Waugh, 2014; Antokhina et al., 2024) and troposphere-stratosphere mass exchange (Holton et al., 1995; Sprenger et al., 2007; Kunz et al., 2015).

Several methods are used to define the effective SPV edge on various pressure and isentropic surfaces. Common approaches include the maximum PV-gradient method (Kunz et al., 2011; Serra et al., 2017), material metrics tracing the separation between tropospheric and stratospheric air masses (Bowman, 1993; Turhal et al., 2024), and constant PV thresholds on given isentropic surfaces (Holton et al., 1995). While each method carries its own merits and limitations, these approaches generally reduce the SPV edge to a one-dimensional boundary, thereby collapsing its finite-width morphology into a single contour. However, the SPV edge is arguably better described as a transient region of enhanced stratospheric tracer gradients (Haynes

https://doi.org/10.5194/egusphere-2026-6696
Preprint. Discussion started: 4 November 2026
© Author(s) 2026. CC BY 4.0 License.

et al., 2000; Neu et al., 2003; Santee et al., 2011), continuously eroded and replenished by eddy–mean-flow interactions. Consequently, one-dimensional edge diagnostics may overlook the nonlinear morphology and finite-width structure of the SPV edge that are fundamental to its interaction with the surrounding flow and, potentially, to stratosphere–troposphere coupling.

While the link between the lower-SPV edge configuration and the subsequent evolution of tropospheric weather systems has been extensively explored (Baldwin and Dunkerton, 2001; Thompson et al., 2002; Black and McDaniel, 2009; Domeisen and Butler, 2020; Hannachi et al., 2025), it remains unclear which lower-SPV edge configurations support the enhanced troposphere-stratosphere coupling deemed necessary to generate the SPV core weakening associated with sudden stratospheric warming (SSW), and their subsequent downward propagation.

SSWs are among the most dramatic events occurring in the atmosphere, marked by an abrupt increase of tens of degrees in mid-to-upper stratospheric temperatures in a manner of days (Baldwin et al., 2021). SSWs are canonically followed by downward propagation of warm anomalies to the upper-troposphere and cold-air outbreaks as displaced SPV airmasses pour into lower latitudes (White et al., 2019 and 2020; Hall et al., 2021a). Beyond their immediate weather implications, changes in their frequency/intensity could potentially act as climate feedback, leading to accelerated polar-ice loss and supporting the positive earth albedo feedback (Mitchell et al., 2012, Xia et al., 2026).

The structure and strength of the SPV affects the upward propagation of planetary waves into the stratosphere, with vortex-edge PV gradients playing an important role in regulating their upward propagation. Consequently, tropospheric wave forcing alone is considered insufficient to explain the onset of SSWs; the stratospheric flow must also provide favourable conditions for wave propagation, focusing, or resonance (Bancala et al., 2012; Albers and Birner, 2014; Yang et al., 2023). The SPV state also affects the development of persistent atmospheric blocking patterns (Hanna et al., 2024), where a stronger SPV is more likely to inhibit or deflect their upward propagation.

As noted by the IPCC (2021), confidence remains low in projections of the Northern Hemisphere stratospheric polar vortex (SPV) response to climate change. Although some studies suggest a weakening of the vortex, its forced response remains difficult to distinguish from internal variability (Seviour et al., 2017), while substantial intermodal spread persists in simulations of its future evolution (Wu et al., 2019). Particularly, models disagree on the sign of future changes in sudden stratospheric warming (SSW) frequency (Ayarzagüena et al., 2020; Gray et al., 2020; Hall et al., 2021b), reflecting uncertainties in both stratospheric radiative responses and tropospheric wave forcing. The competing effects of enhanced CO_2-induced stratospheric cooling and changes in tropospheric and Arctic temperature gradients further complicate the response (Lin and Emanuel, 2024; Cohen et al., 2026). Consequently, substantial uncertainty remains in how climate change will alter SPV stability and its coupling to the troposphere. Improving these projections therefore requires a better understanding of SPV variability, both to distinguish the climate response from intrinsic variability and to identify the pathways leading to SPV instability, including the role of nonlinear Rossby-wave breaking in modulating planetary-wave forcing (Lawrence and Manney, 2018).

https://doi.org/10.5194/egusphere-2026-6696
Preprint. Discussion started: 4 November 2026
© Author(s) 2026. CC BY 4.0 License.

In this study, we aim to characterize recurring lower-SPV edge configurations based on their PV morphology and investigate the associated surface weather anomalies and SPV-core perturbations, establishing a PV based perspective on troposphere-stratosphere coupling. The objectives of this study are:

1. Detect dominant, recurring patterns of the lower-SPV edge based on reanalysis data
2. Characterize the perturbations associated with each pattern from the surface to the stratosphere
3. Reveal preferred dynamical pathways leading to SPV weakening and potential SSWs

Rather than delineating a point-wise boundary, we define the lower-SPV edge as the region bounded between quantized PV values, classifying daily SPV edge morphologies into 12 groups based on their objective similarity using a self-organizing map (SOM, Kohonen, 1990). This measure naturally handles non-linear RWB formations such as elongated PV streamers and cut-offs, allowing the SOM algorithm to detect and trace their signal. This approach highlights the observed dominant lower-SPV states and their interactions with the stratosphere and troposphere.

The SOM analysis is growing popular for atmospheric applications (Hewitson and Crane, 2002; Sheridan and Lee, 2011; Wichrowski et al., 2026), as a useful tool to decompose a continuum of system states into coherent, recurring patterns, and visualize transitions between them. Among others, the present analysis draws heavily on previous SOM studies applied to PV fields (Givon et al., 2021; 2024), as well as on Berkovic et al. (2021), whose work demonstrated the ability of SOM analysis to extract coherent three-dimensional large-scale patterns from local one-dimensional datasets.

The study is structured as follows: Section 2 provides details of the lower-SPV edge definition, SOM analysis, transition persistency analysis, wave-activity flux calculations, lead-lag regression analysis, and anomalous node occupancies conditioned by SSWs. Section 3 opens with the detected SOM patterns and their characteristics, followed by the transition-persistency results, Eddie-mean flow interactions, and finally, evaluate the lower-SPV edge relationship with the SPV itself.

2. Methodology

2.1. Lower-SPV edge definition

We hereby develop a novel perspective used to define the lower-SPV edge and identify its recurring configurations. We focus on the 350 K isentropic surface for several reasons: first, its location above the tropopause enables a year-round classification of the SPV edge, with no concern of interaction with topography. Second, the 350 K iso-surface lies far enough above the tropopause to avoid contamination by precipitation and tropopause folding, while still "sensing" the impact of the tropospheric jet from below. Third, its stratospheric position suggests more conservative (adiabatic) conditions in terms of PV. Above all, the lower stratosphere is perceived as the "gateway" for tropospheric impact on the stratosphere, making it a natural choice for the present study. We identify equivalent latitudes and maximum PV gradient bands on the 350 K surface, and select the 6-7 PVU interval as it best follows these classic SPV edge definitions, albeit with the additional advantages of (i) PV conservation

https://doi.org/10.5194/egusphere-2026-6696
Preprint. Discussion started: 4 November 2026
© Author(s) 2026. CC BY 4.0 License.

under adiabatic conditions reassures physical comparability at all instances, and (ii) the ability to relate morphological structures with jet intensity via the strong correlation between the meridional PV gradient (here marked by the distance between the 6 and 7 PVU contours) and the magnitude of the zonal wind (Buckenberger et al., 2023).

Therefore, instead of treating the lower-SPV edge as a finite border with a single latitude for each longitude, we define the edge as a dynamical, 2-D feature that allows varying engulfed area, constrained by PV conservation. Under the proposed PV-band approach, the SPV edge morphology also reflects the local jet intensity, providing meaningful and dynamically interpretable flow regimes. The dynamical definition of the 6-7 PV-band as the lower-SPV edge was further motivated by the insightful work by Davies and Sprenger (2026), that demonstrated the value of analysing annular PV features along the SPV edge. The 6–7 PVU interval also encompasses the climatological maximum PV-gradient region on 350 K, thereby providing a finite-width representation of the lower-vortex boundary, as shown in Fig. A2.

In preliminary analysis, various alternative lower-SPV edge definitions were examined. Those include classifying the full 350K PV field, as well as classifying by single PV contours, and by the maximum PV gradient. While the full PV field emphasized Arctic PV magnitudes, the latter two delivered similar, limited morphological insight with PV anomalies concentrated along the parameter of choice (Fig. A1). The classification resulting from the single-contour approach is discussed in Appendix A as further support for selecting the double-PV contour framework.

2.2. SOM analysis

Building on previously established uses of self-organizing map (SOM) applied to the isentropic PV field for the study of Mediterranean cyclones (Givon et al., 2021, 2024, 2026), we apply the SOM to the 6-7 PVU band on the 350K iso-surface in a hemispheric, daily, year-round analysis, thereby essentially treating the SPV as a single, large-scale cyclone. The study is based on ECMWF (European Centre for Medium-Range Weather Forecasts) ERA5 reanalysis data (Hersbach et al., 2020) for years 1979-2024.

We follow the “elbow method” (Wang et al., 2013) to evaluate SOM errors by changing the number of SOM nodes (N) and averaging mean-squared errors within each node and across the SOM lattice, establishing N=12 as a local minimum in SOM error per added node. Adding further nodes reduced the SOM learning rate significantly. We thus obtain 12 groups, each representative of daily-scale recurring patterns, with mean frequencies ranging from 3% for rare winter modes to 28% for the summer period, when the 350K surface effectively detaches itself from the tropopause as it is lifted by the seasonal radiative heating. We further utilize composite analysis and statistical testing to validate the robustness of the detected patterns and their associated weather implications.

2.3. Transition-persistency analysis

To identify dominant pathways within the SOM lattice, we analyze transition-persistency statistics using a Monte-Carlo statistical testing. The transition-persistence frequencies demonstrate the temporal persistency of the detected SOM nodes as

https://doi.org/10.5194/egusphere-2026-6696
Preprint. Discussion started: 4 November 2026
© Author(s) 2026. CC BY 4.0 License.

well the limited statistically allowed transitions, highlighting the enhanced SPV-edge predictability under the proposed framework. Each day in the analysis period is associated with a particular SOM node. Consecutive days identified as the same SOM node are counted as persistency, while a node-shift is registered as a transition. Specifically, we re-generate a thousand random permutations of the transition-only data, marking transitions that surpass the 95th percentile threshold as statistically significant in the 95% confidence level.

2.4. Eddie-statistics and wave activity fluxes

To investigate the eddy-mean flow interactions captured by the detected lower-SPV-edge configurations, and highlight the capability of each to perturb the SPV, we analyze nodal composite-means of eddy momentum flux ($\overline{u'v'}$) and meridional heat flux ($\overline{v'\theta'}$), complemented by the transient wave activity flux (following Plumb 1986, Eq. 2.24):

(1) $$M_r = \frac{p\cos(\varphi)}{\bar{u}_{mag}}\begin{bmatrix} \bar{u}(v'^2 - E) - \bar{v}(u'v')\hat{\imath} \\ \bar{v}(u'^2 - E) - \bar{u}(u'v')\hat{\jmath} \\ \frac{f}{d\bar{\theta}/dz}\left(\bar{u}(v'\theta') - \bar{v}(v'\theta')\right)\hat{z} \end{bmatrix}$$

Where E denotes eddy kinetic energy, u, v the zonal and meridional winds, θ denotes the potential temperature, and $\bar{u}_{mag}$ denotes the magnitude of climatological winds. Following Plumb 1986, primes ($'$) denote daily deviations from monthly-gridded climatology, marked by an overbar ($\bar{u}, \bar{v}, \bar{\theta}$).

While eddy fluxes highlight the tropospheric "storminess" associated with each SOM node, the latter Plumb fluxes (M_r) mark the preferred directionality of Rossby-wave propagation in three-dimensional space, with the divergence denoting regions of Rossby wave sources and sinks. This measure particularly reveals which regional forcings tend to break the lower-SPV-edge barrier and penetrate to the stratosphere, where it can drastically decelerate westerly winds and destabilize the SPV.

2.5. Transition-anchored lead-lag analysis

To elucidate the upper SPV response and preconditioning to lower-SPV edge configurations, we apply a lead-lag composite analysis centred around nodal transitions. Specifically, for each entry into node j, the ±30 day zonal-mean zonal winds at 60°N on the 10 hPa level are composited and contrasted with the climatological composites of the corresponding dates. Specifically, for each lead/lag time, both the climatological values and anomalies are averaged, with the absolute wind expressed as the sum of the two. Thus, the perturbations associated with each node are compared to the equivalent climatology – quantifying both the anomalies and absolute winds. The mean zonal wind speed at node transition times is reported, along with the correlation coefficient and standard deviations across the lead-lag time. Thus, the two-way coupling of the lower-SPV edge modes to the SPV-core is evaluated.

https://doi.org/10.5194/egusphere-2026-6696
Preprint. Discussion started: 4 November 2026
© Author(s) 2026. CC BY 4.0 License.

2.6. Anomalous nodal occupancy around SSWs

To highlight the link between the detected lower-SPV edge patterns and the occurrence of SSWs, we analyze nodal occupancy anomalies in the weeks preceding and following SSW events, which we define based on the reversal of zonal-mean zonal winds at 60°N, 10 hPa, occurring in DJF.

For each SSW event, the nodal occurrence distributions are contrasted with the monthly climatological frequencies, showing anomalously high/low occurrence of specific SOM nodes before and after SSW events. Combined with the lead-lag regression, these results reveal the dynamical evolution of SSWs from the lower-SPV edge perspective.

3. Results

3.1. Detected lower-SPV edge patterns

The SOM-detected lower-SPV edge patterns and the corresponding 350 K isentropic PV and surface pressure anomalies are presented in Figure 1. The 12 nodes can be qualitatively binned into 3 groups: seasonal emphasis, regional blocking patterns, and annular-hemispheric nodes. While the upper row shows a seasonally oriented separation between two prominent summer nodes (nodes 1 and 2) and two autumn-spring dominant nodes (nodes 3 and 4, respectively), the remaining 8 nodes demonstrate a dynamical separation of recurring winter-time flow configurations on a shorter temporal scale. Indeed, while the summer node (1) occupies ~28% of the year, some of the detected winter modes show annual frequencies as low as 2%. The hemispheric-annular group portrays a diffused lower-SPV edge (node 6), with negative PV anomalies along the edge and positive within the polar cap, and the opposing, sharp SPV edge (node 7) featuring positive PV anomalies along the edge and negative about the pole. Similar annular modes were highlighted by Black and McDaniel 2009 as a Polar Annular Mode (PAM), associated with tropospheric temperature anomalies comparable to the well-established stratospheric northern annular mode (SNAM). Coherent weak lower-SPV is associated to node 10, with negative PV anomalies across the polar circle, while a primarily standalone Atlantic positive PV anomaly dominates node 8. The regional blocking nodes include well-known regional weather patterns, namely the Scandinavian, North-Pacific, Greenland, and Alaskan blockings, denoted by nodes 5, 9, 11, and 12, respectively (Barriopedro et al., 2006; Tyrlis and Hoskins, 2008; Dunn-Sigouin et al., 2013; Tibaldi and Molteni, 2018). Sea-level pressure (SLP) anomalies (black contours in Fig. 1) demonstrate the coherent response of the near-surface circulation regimes associated to each lower-SPV edge class, canonically showing negative SLP (cyclonic) anomalies interacting with positive PV anomalies, and positive SLP anomalies (anti-cyclonic) interacting with negative PV anomalies. Some annual-mean nodal frequencies show considerable changes between the first and second halves of the reanalysis period (1979-2024), implying that certain flow configurations may be shifting in dominance, although further analysis is required for attribution to anthropogenic forcing.

https://doi.org/10.5194/egusphere-2026-6696
Preprint. Discussion started: 4 November 2026
© Author(s) 2026. CC BY 4.0 License.

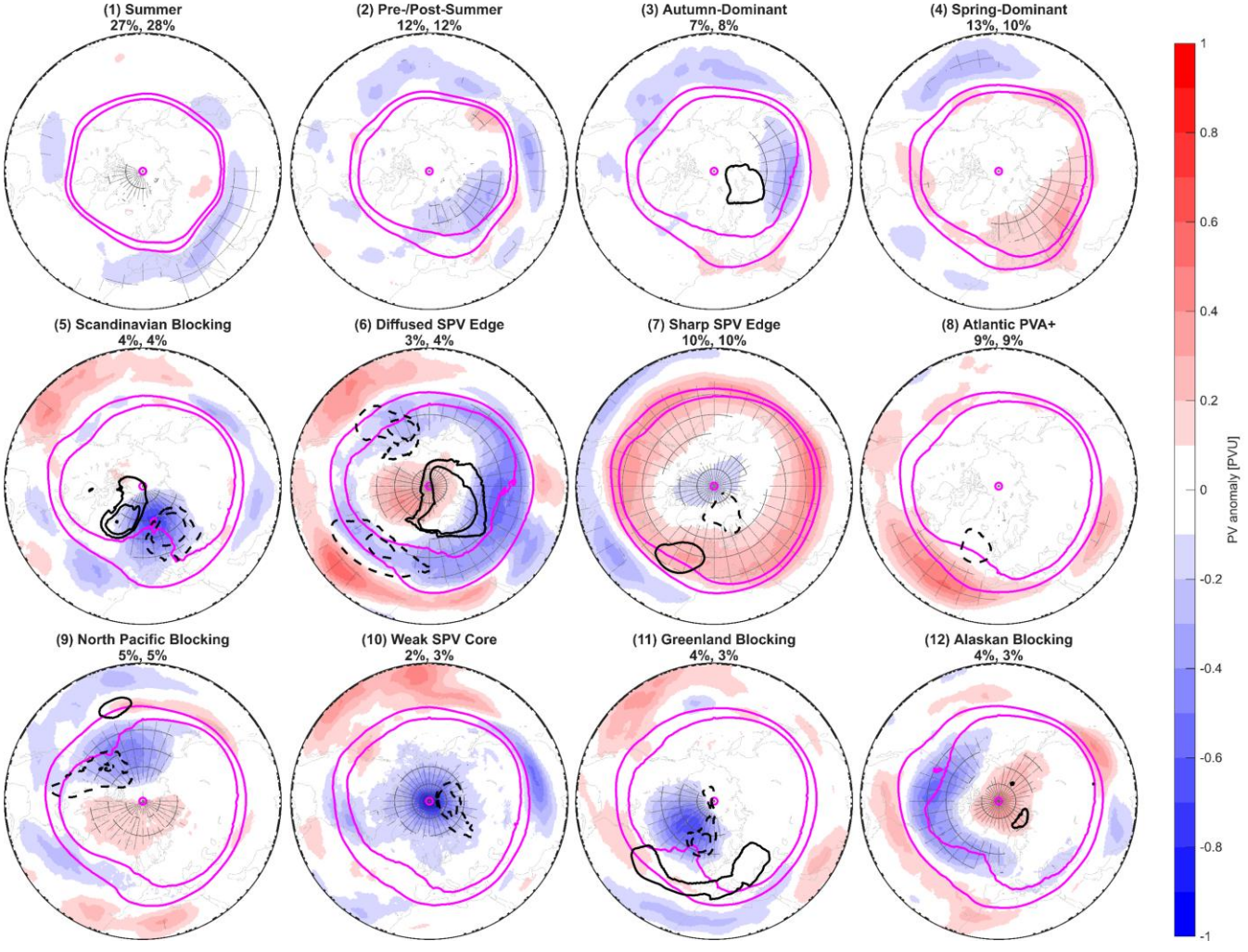


Figure 1. Self-organizing map (SOM) nodes of the 6–7 PVU contours on the 350 K isentropic surface used as the classification agent (magenta contours). Shading shows composites of PV anomalies on the 350 K isentropic surface, while dashed/solid black contours indicate SLP anomalies of +2, +4 and -2, -4 hPa, respectively. All anomalies are defined relative to the monthly gridded climatology. Statistically significant PV anomalies (95% confidence level) are stippled, whereas only statistically significant (95%) SLP anomalies are shown. Panel titles indicate the dominant feature associated with each SOM node, together with the mean occurrence frequency during the first and last 23 years of the reanalysis period.

2-meter temperature anomalies shown in Fig. 2 further demonstrate the instantaneous surface imprint of each node. Notably with the contrasting nodes 6 and 7 showing a warmer/colder Europe related to diffused/sharpened SPV edges, respectively. Upper-level geopotential anomalies reflect the instantaneous imprint of the lower-SPV edge configuration on the SPV. From the 10 hPa geopotential heights distribution, the SPV appears exceptionally strong/weak under specific nodes: shallowest in the off-winter nodes (nodes 1, 2, and 4), with deeper lows in nodes 6, 9 and 12, and shallower ones in nodes 5, 7, and 10.

https://doi.org/10.5194/egusphere-2026-6696
Preprint. Discussion started: 4 November 2026
© Author(s) 2026. CC BY 4.0 License.

Moreover, hints of a shifted/split SPV are evident in nodes 10 and 11, although this association cannot be determined from the composite means alone, and require further analysis. Overall, Fig. 2 demonstrates coherent atmospheric variations from the 10hPa level all the way to the surface, as determined solely from the lower-SPV edge morphology.

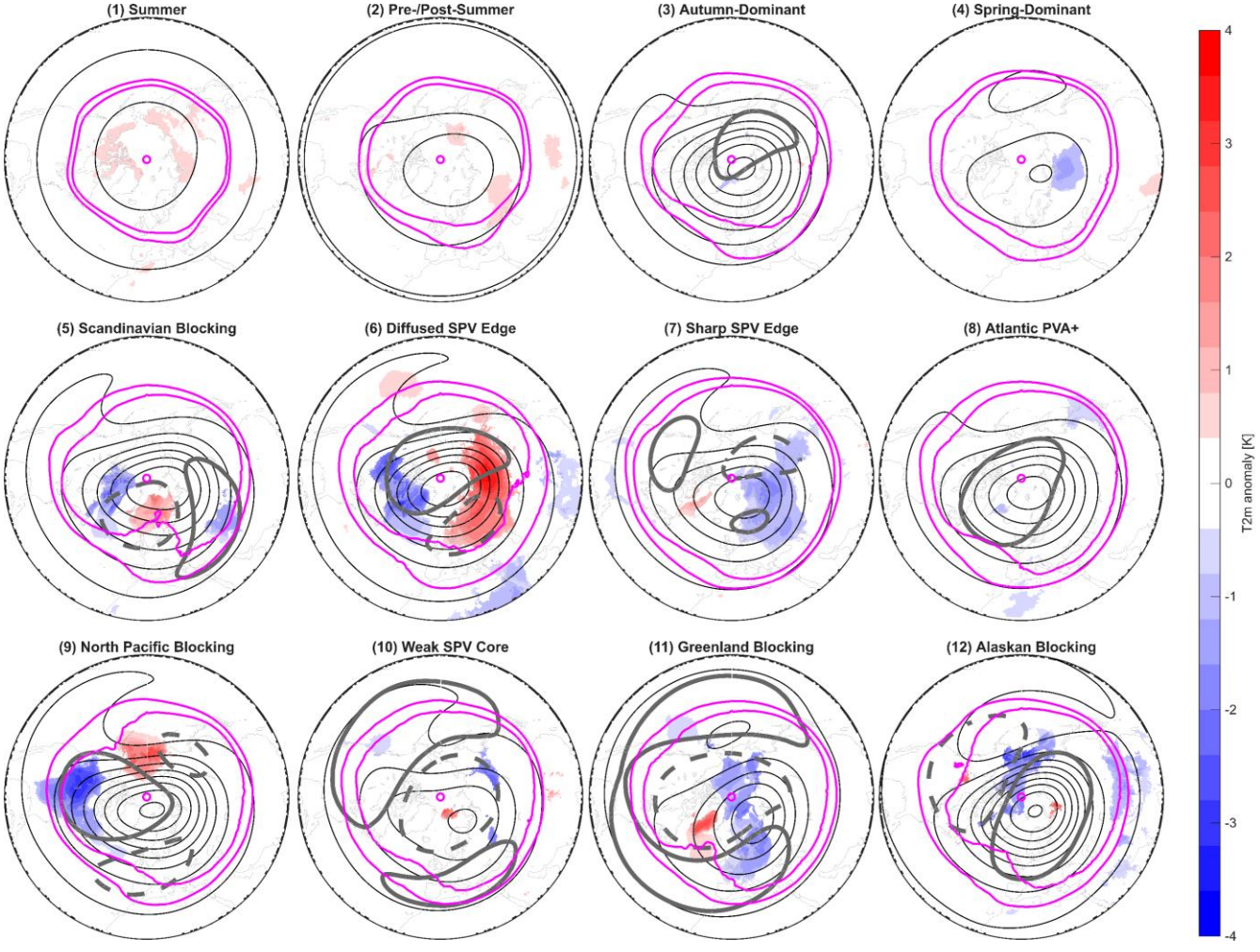


Figure 2. As in Figure (1) but showing 10 hPa geopotential heights (black contours, 250 m intervals) and geopotential height anomalies (dashed/solid grey contours for positive/negative 500 m anomalies). Shading denotes the corresponding statistically significant (95%) 2-meter temperature anomaly composites. The magenta contours are as in Figure 1.

The monthly distribution of the SOM nodes is presented in Fig. 3. Node 1 essentially occupies the entirety of July and August – with the occasional involvement of node 2. The second most seasonally dependent nodes are 2 and 4, occupying ~ 54% of October and ~58% of May, respectively, while showing considerable amplitudes in other months as well. Node 3 also occurs predominantly during Autumn, with a continuous yet weak amplitude across winter. The other 8 winter nodes are more evenly spread across the extended winter period, when the bulk of SPV variability occurs. In other words, the results do not converge

https://doi.org/10.5194/egusphere-2026-6696
Preprint. Discussion started: 4 November 2026
© Author(s) 2026. CC BY 4.0 License.

to a seasonal decomposition – rather, the nodes are linked to a dynamically meaningful pattern with comparable monthly amplitudes, despite a slight tendency towards each node's favoured months.

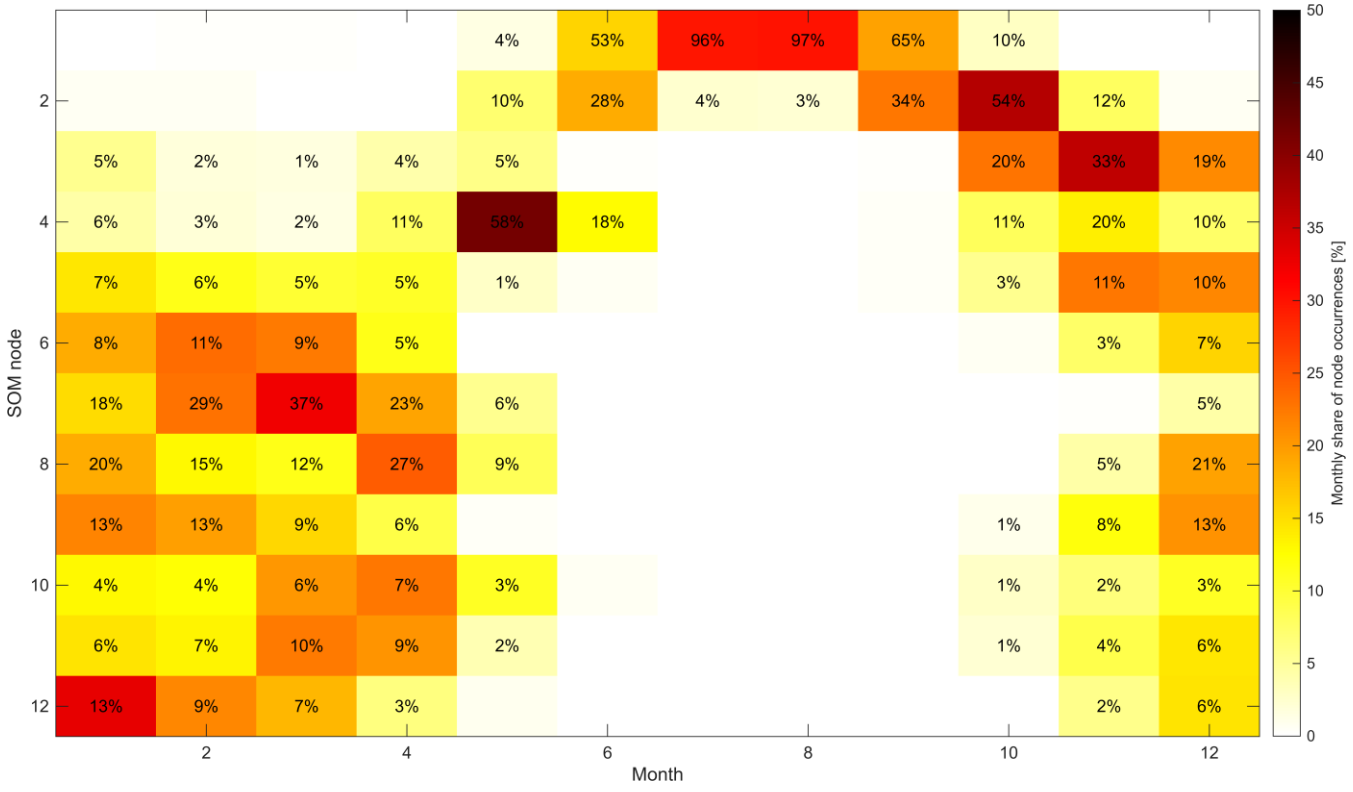


Figure 3: Seasonal distributions of SOM nodes relative to total node entries (shading, %). Percentages in each cell report the nodal share of each corresponding month.

To better understand whether changes in annual nodal frequencies are a part of a coherent long-term trend, 10-year running-mean node frequencies are quantified, and the existence of linear trends is verified using a Mann-Kendall test at the 95% confidence level. SOM nodes that show a change in annual-mean frequencies in the early and late halves of the analysis period (Figure 1) also show a significant, long-term trend, with the sharpest decrease shown for the Spring-dominant node (4) with negative 35% per decade (-0.42 days per year), followed by an increase of 70% and 100% per decade (~0.25 days per year, each) for the diffused SPV Edge and Weak SPV nodes respectively (6 and 10). The annual frequency of summer node (1) also increases by 9% per decade (0.25 days per year), possibly pointing to the extension of Summer at the expense of Spring in recent decades. While further analysis is required to attribute these trends to climate change, the results show meaningful long-term changes in nodal frequencies that can potentially act as a climate feedback mechanism.

https://doi.org/10.5194/egusphere-2026-6696
Preprint. Discussion started: 4 November 2026
© Author(s) 2026. CC BY 4.0 License.

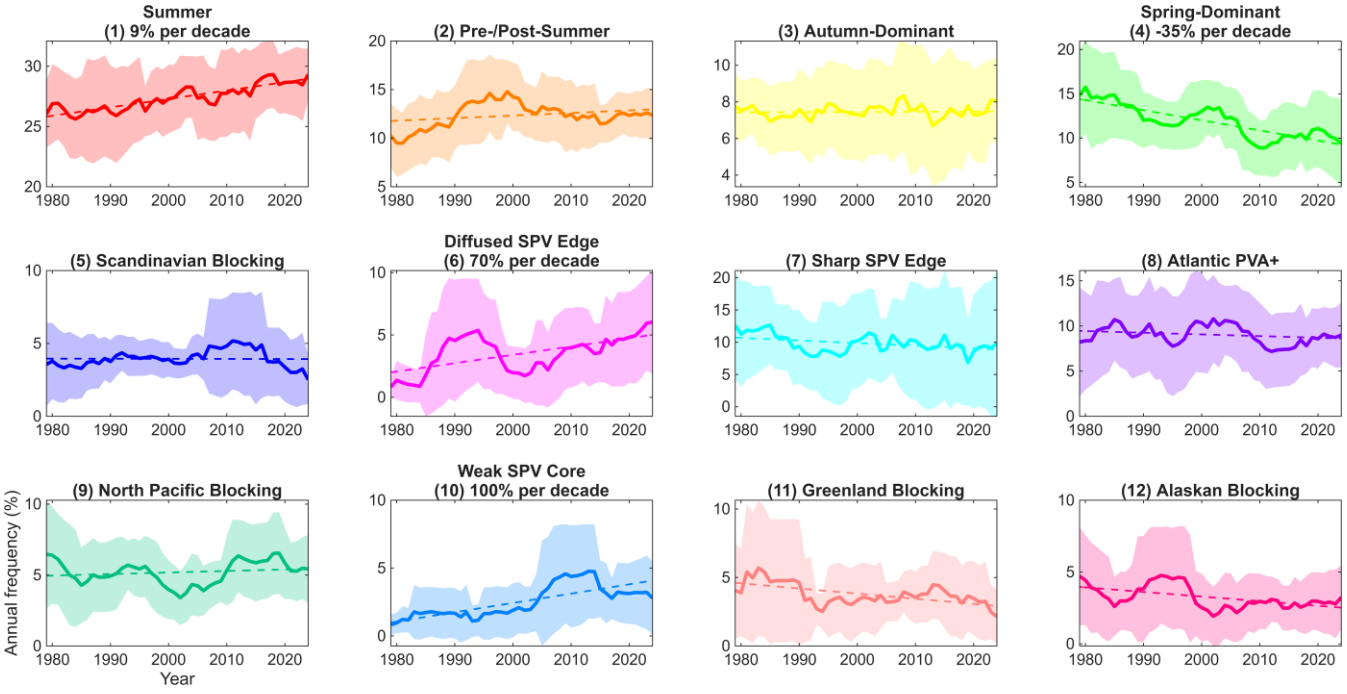


Figure 4: 10-year moving means (solid lines) ±1 standard deviations of annual SOM node frequency. Titles denote the SOM-node. The slope of the observed trend in days per year is shown for nodes that pass a Mann-Kendal test for the existence of a linear trend at the 95% confidence level.

To illustrate the added value of defining the SOM using two PV contours rather than a single contour, Fig. 5 shows the distribution of the area enclosed by the 6–7 PVU annulus for each SOM node. The SPV-edge area clearly represents one of the principal characteristics distinguishing the circulation regimes. Each node exhibits a distinct distribution of SPV-edge area, with the largest median areas associated with the diffused SPV-edge regime (node 6), followed by the Alaskan blocking regime (node 12). In contrast, the smallest areas are found during the summer and spring-dominant regimes (nodes 1 and 4) and in the sharp SPV-edge regime (node 7). The relatively limited overlap among the distributions indicates that the SOM effectively separates circulation states according to SPV-edge width, a distinction that would not be captured using a single PV contour and would similarly be lost using too many PV contours (or the full PV field).

The SPV-edge width results also provides insight into when the SPV acts as a dynamical transport barrier. A narrower (sharper) PV band corresponds to a stronger potential vorticity gradient, which inhibits isentropic mixing across the vortex edge and more effectively isolates the polar cap. Such isolation favours the maintenance and intensification of positive polar PV anomalies, whereas a broader (more diffuse) SPV edge is indicative of enhanced mixing between polar and midlatitude air masses and the development of negative polar anomalies. Hence, nodes with a larger SPV edge area are potentially more susceptible for tropospheric perturbations – while nodes with smaller SPV area are expected to reflect perturbations downward through enhanced jet and vertical shear. This notion is further discussed in Section 3.4

https://doi.org/10.5194/egusphere-2026-6696
Preprint. Discussion started: 4 November 2026
© Author(s) 2026. CC BY 4.0 License.

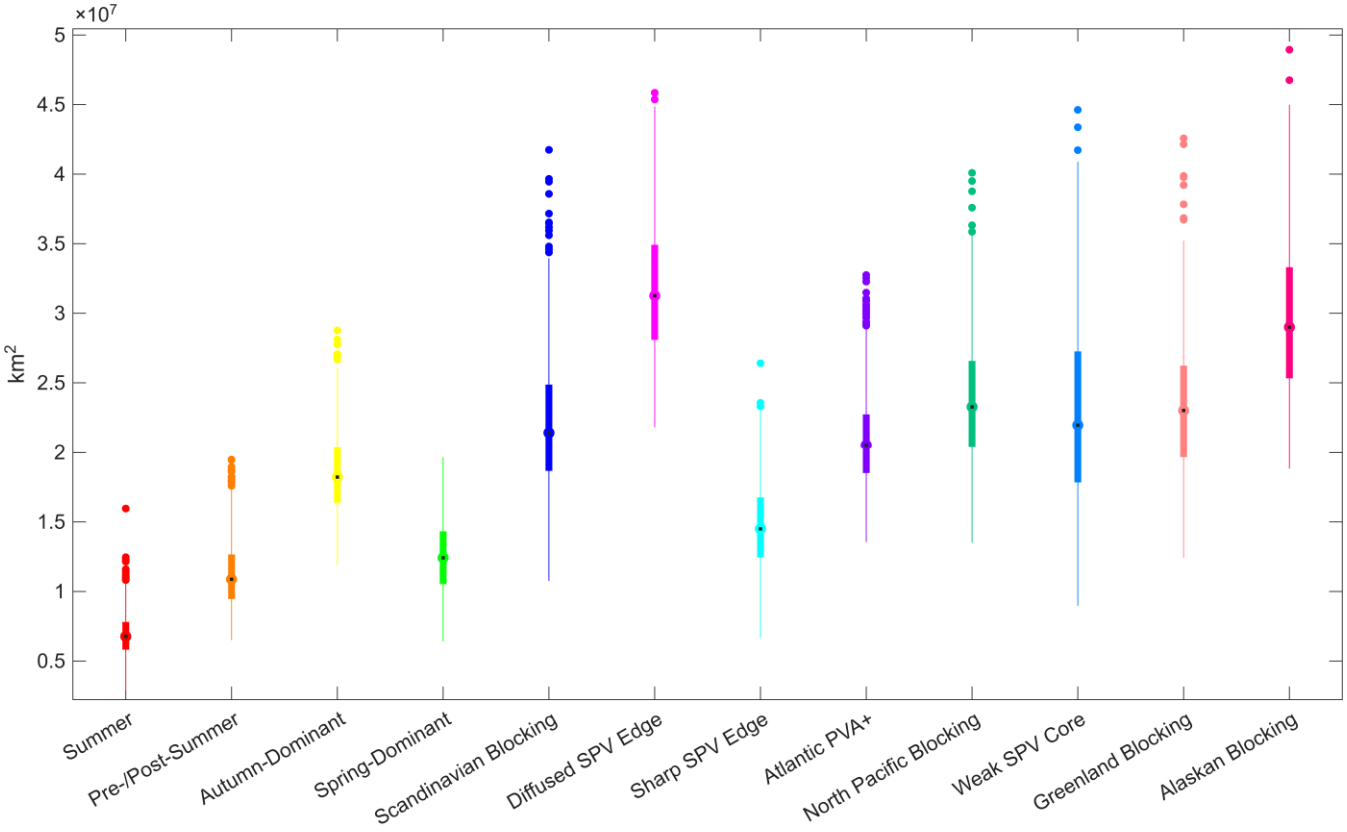


Figure 5: Boxplots showing the distribution of SPV-edge area across the SOM nodes. The boxes denote the 25th -75th percentiles, while whiskers denote the 97.5 and 2.5 percentiles, marking the limits for the outliers marked by coloured dots.

3.2. Transition-Persistency analysis

The transition-persistence matrix shown in Fig. 6 illustrates the varying degrees of nodal persistence along the main diagonal and highlights statistically preferred transition pathways in the off-diagonal elements. The summer node (1) clearly shows the highest persistency (~90%), whereas node 5 exhibits the lowest, with only ~40% of node days persisting in the same state. The remaining nodes display comparable persistence of approximately 50%. Interestingly, while neighbouring SOM nodes tend to be more similar, many of the secondary diagonals that represent transitions into neighbouring nodes are not statistically significant. Instead, several transitions between more distant nodes occur preferentially. Examples include the 11→5 transition, highlighting the connection between the Greenland and Scandinavian blocking regimes, and the particularly common 9→12 transition, linking the North Pacific and Alaskan blocking regimes. The weak SPV core (node 10) is preceded primarily by nodes 5, 7, 9. and 11, associating Scandinavian, North-Pacific, and Greenland blockings, as well as the sharp SPV-edge configurations, with an imminent lower-SPV weakening. In winter, the sharp SPV edge configuration – that is also linked to a weakened lower SPV core – predominantly arises from the Atlantic PVA+ node 8. This link reflects a PV redistribution

https://doi.org/10.5194/egusphere-2026-6696
Preprint. Discussion started: 4 November 2026
© Author(s) 2026. CC BY 4.0 License.

following strong cyclonic activity, where PV concentrates along the lower SPV edge, at the expense of the core PV reservoir. As discussed in Davies and Sprenger, 2026, such an annular mode of enhanced edge PV gradients can lead to SPV instability and a potential rapid SPV breakdown. Thus, the transition 7→8 showcases a recurring scenario of SPV weakening that does not require the formation of persistent atmospheric blocking.

Overall, the TPM reveals that transitions between SOM nodes are far from random: each node evolves through a limited number of statistically preferred pathways, indicative of distinct regime transitions. Seasonal conditioning further restricts these transient pathways (not shown), given the seasonal distribution of the different SOM nodes. Moreover, the secondary-transition analysis indicates that node transitions also depend on the previous transition history, rather than on the current node alone. E.g., node 9 is likely to transit into nodes 3/8 if preceded by node 3, or to node 12 if preceded by node 6. In many cases, the system tends to transit back to the original node, e.g., node 10 tends to switch back to node 5, 7, or 9 after transitioning from them. These pathways may provide a basis for future studies on predictability and dynamical model-evaluation. Together, these results suggest that the evolution of the lower-SPV edge is governed by a constrained set of physically meaningful transition pathways.

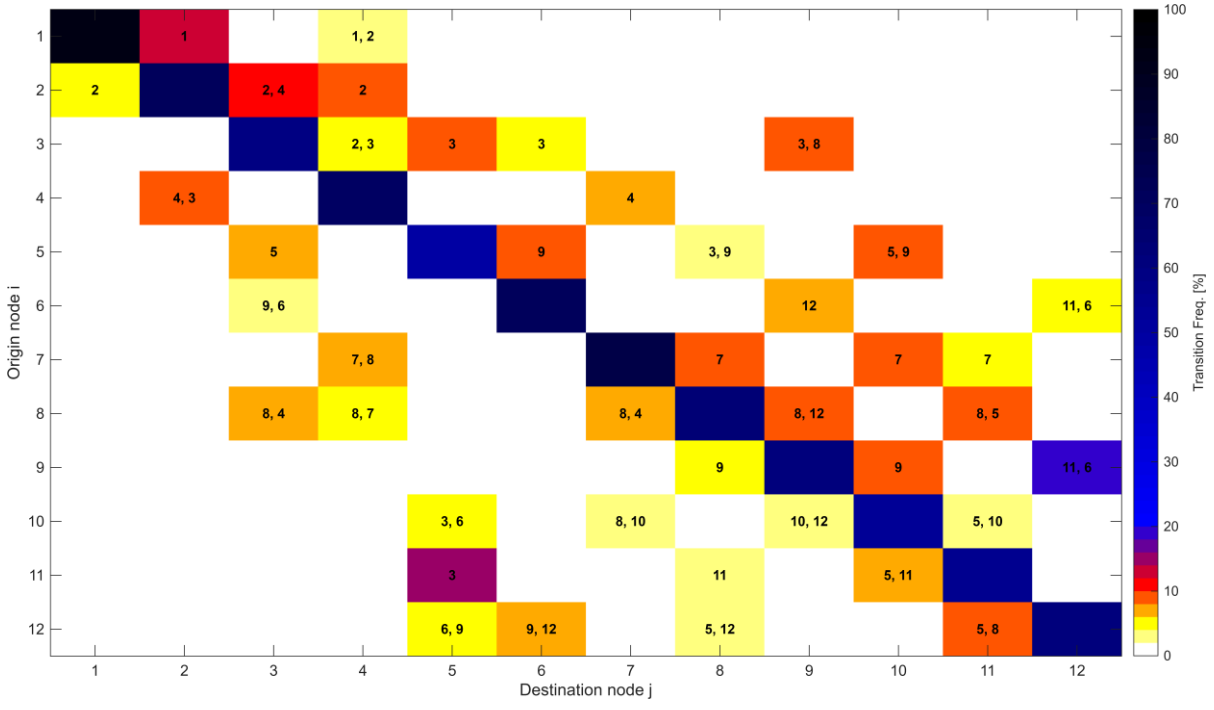


Figure 6: Persistence-transition matrix. The y-axis denotes the previous node, and the x-axis denotes the next node. Shading marks the ratio between each transition to the total number of node entries, so that each row adds up to 100%. Only transitions above the 95% confidence level are shown. Numbers indicate the prominent secondary transitions (probability>20%) following transition i→j.

https://doi.org/10.5194/egusphere-2026-6696
Preprint. Discussion started: 4 November 2026
© Author(s) 2026. CC BY 4.0 License.

3.3. Eddy–mean-flow interactions

To analyze the differing eddy–mean flow interactions dominating each SOM node, Fig. 7 shows the transient eddy heat flux anomalies relative to monthly gridded climatology. Transient wave activity fluxes (eq. 1, following Plumb 1986) are shown to denote the propagation of transient eddies. While variations in wave propagation appear mild, eddy heat fluxes are shown to peak primarily under the blocked-flow configurations (nodes 5, 11, and 12) as well as under diffused SPV edge (node 6) and the weak SPV core (node 10). For the blocking regimes, this result is likely due to the geographical consistency of eddy heat flux within the node members, while for nodes 6 and 10, these results indicate the enhanced upward propagation associated with the nodal primary features – namely, the weakened dynamical barrier posed by the weak SPV edge and core. Nodes 7 and 8, representing less perturbed SPV states, show much weaker eddy heat fluxes and a smoother, more symmetric waveguide.

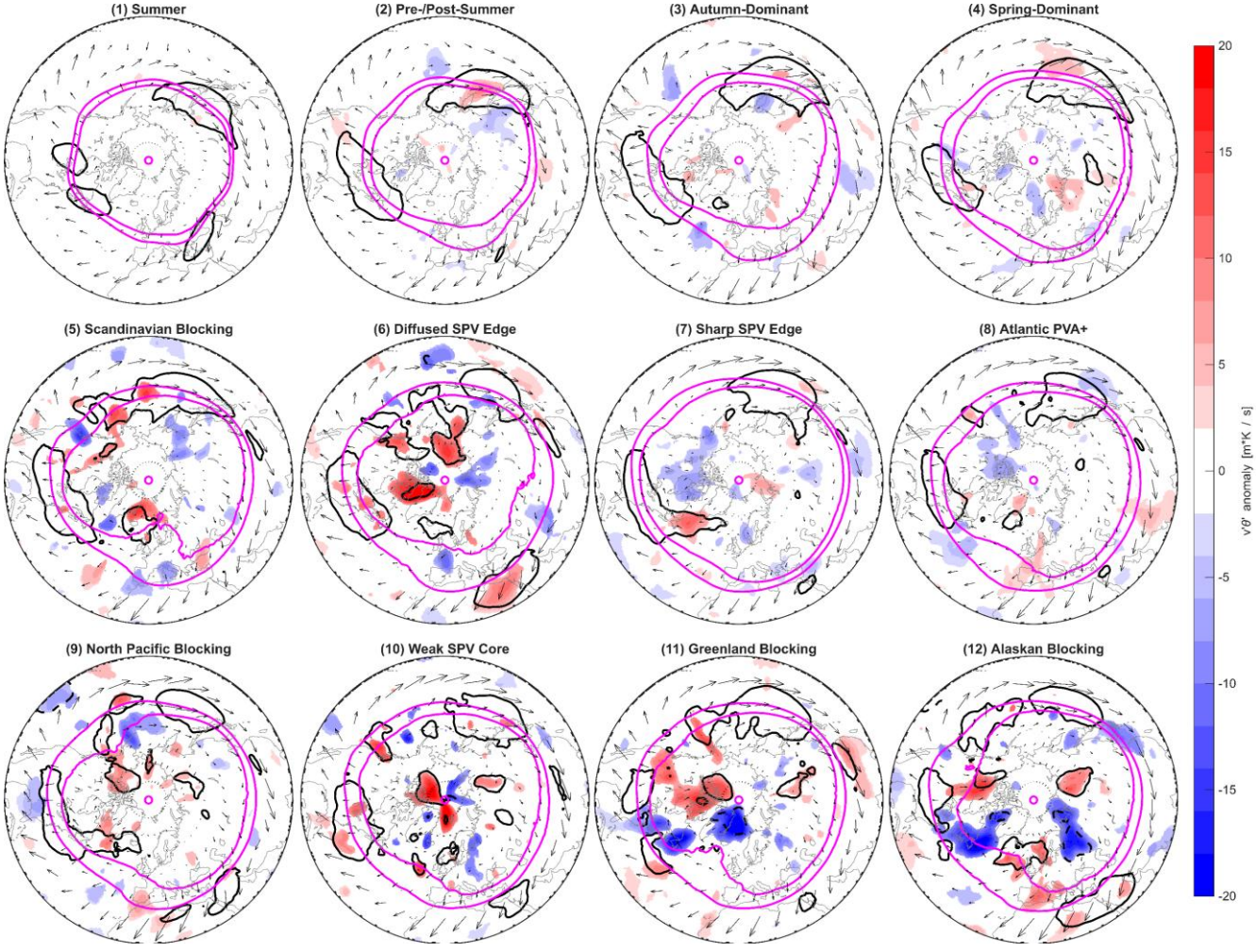


Figure 7: $\overline{v'\theta'}$ anomaly composites on the 250 hPa level (shading, filtered at the 95% confidence level). Vectors denote the horizontal components of the total transient wave activity flux on the 250 hPa level. Black contours indicate ±15 [m*K/s] mean values, dashed for negative. The magenta contours are as in Figure 1.

https://doi.org/10.5194/egusphere-2026-6696
Preprint. Discussion started: 4 November 2026
© Author(s) 2026. CC BY 4.0 License.

Fig. 8 shows that the spatial patterns are readily transmitted to the zonal mean, with distinct and often opposing anomalies associated with the different winter nodes. While the upper row generally shows weak anomalies, the winter nodes exhibit extensive variability. The relatively unperturbed Atlantic PV+ anomaly (node 8) shows the weakest eddy heat and momentum flux anomalies, followed by the sharp SPV edge captured by node 7. The strongest, positive heat fluxes consistently occur in the polar lower-stratosphere under the diffused SPV edge (node 6), and under North-Pacific blocking (node 9). In contrast, the strongest, negative Eddy heat and momentum fluxes are detected for the Greenland and Alaskan blocking configurations (nodes 11 and 12, respectively). Interestingly, North-Pacific blocking (node 9) generates robust zonal-mean anomalies despite milder regional spatial variations, highlighting the fundamental difference between its blocking geometry compared to node 6's annular morphology. The results therefore point to the diffused SPV edge and North-pacific blockings (nodes 6 and 9, respectively) as strongly associated with SPV weakening. We further evaluate the vertical component of the transient wave activity to consolidate this conclusion.

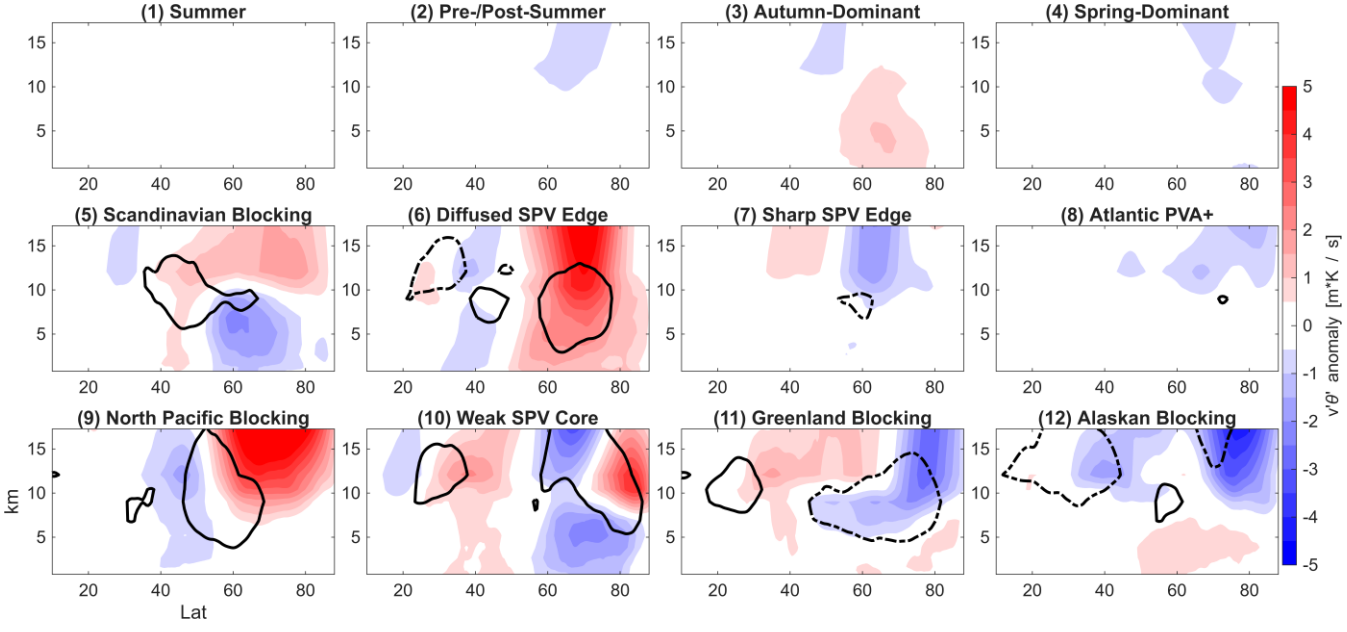


Figure 8: Meridional-vertical cross-sections of $\overline{v'\theta'}$ anomaly (shading). Black contours denote $\overline{u'v'}$ anomaly ($\pm 2\,\frac{m^2}{s^2}$) with dashed contours indicating negative values.

The vertical component of the transient wave-activity flux quantifies the upward propagation of transient eddies to the stratosphere. In agreement with Figs. 7 and 8, Fig. 9 shows that the strongest upward propagation is also associated with nodes 6 and 9, with the Alaskan blocking (node 12) contributing similar positive anomalies, albeit more balanced with negative anomalies. As for the eddy heat flux, nodes 1-4 and 7-8 show the weakest vertical propagation, with considerable contributions from nodes 5, 10, and 11. The zonal-mean results displayed in Fig. 10 are particularly revealing – not only do the waves penetrate deepest into the stratosphere in nodes 6 and 9 – different vertical structures are shown across the mid-latitudes, with significant downward wave reflection under Scandinavian blocking (node 5) giving way to upward propagation in node 6, and

https://doi.org/10.5194/egusphere-2026-6696
Preprint. Discussion started: 4 November 2026
© Author(s) 2026. CC BY 4.0 License.

opposing anomaly dipoles alternating between nodes 9 and 10. Overall, a tight dependency is shown to exist between Rossby-wave propagation and the configuration of the lower-SPV edge, emphasizing the relevance of the PV-band framework to eddy-mean flow interactions.

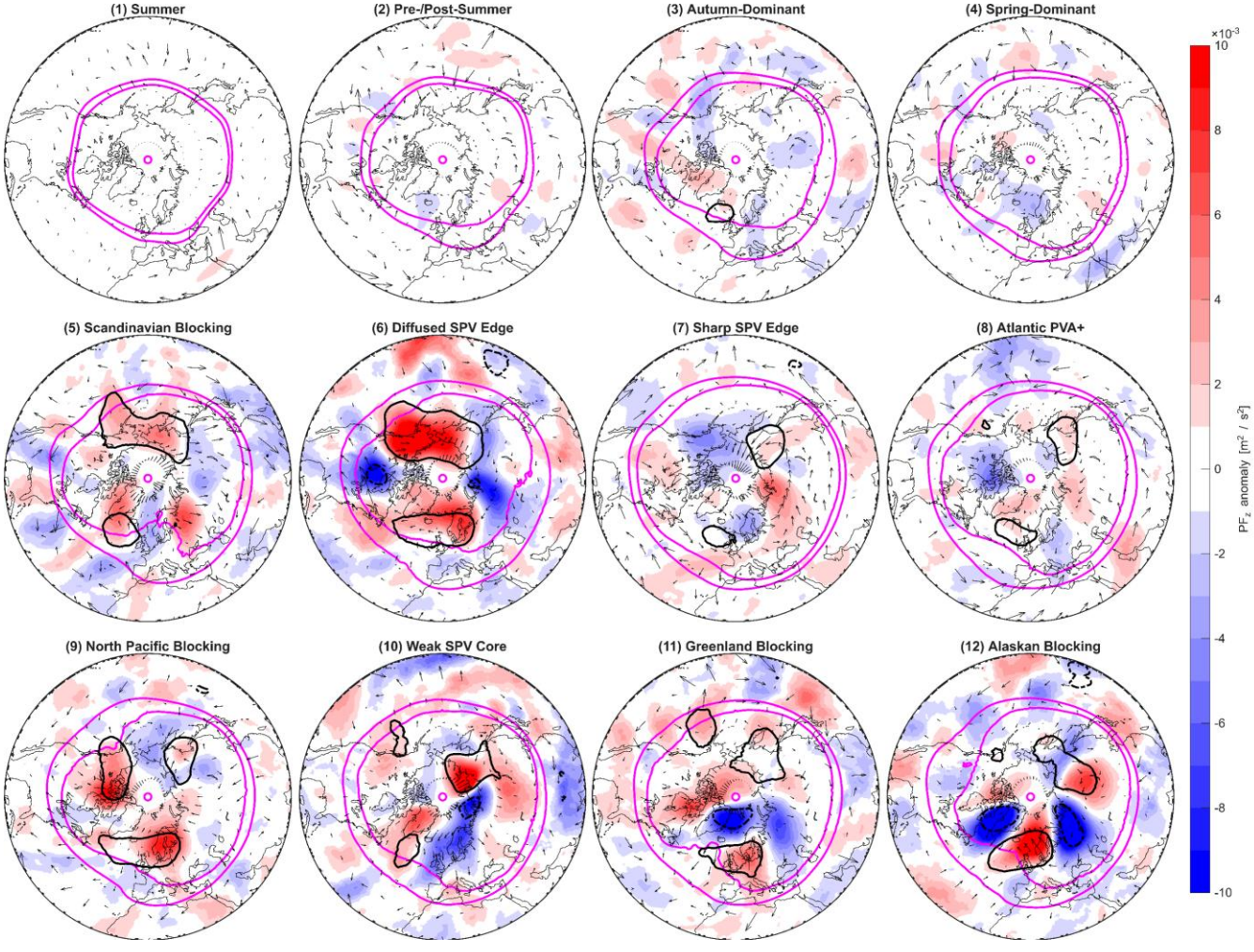


Figure 9: Transient wave activity flux anomaly composites on the 100 hPa level. Anomalies in the vertical component are shown in shading, whereas arrows denote the horizontal anomalies. Black contours show the nodal-mean PFz ($\pm$ 0.01 m^2/s^2) with dashed contours indicating negative values. The magenta contours are as in Figure 1.

The wave activity flux anomalies provide insight into the propagation pathways through which planetary waves may influence the SPV: Enhanced vertical wave propagation into the stratosphere is generally associated with SPV deceleration, whereas changes in horizontal propagation may alter wave forcing in the subtropics and thereby influence the Brewer–Dobson circulation (BDC, Butchart 2014). In particular, the reduced wave propagation through the upper tropical atmosphere in nodes 5, 6, and 12 is consistent with a weakened BDC, which may in turn affect the strength of the SPV. The eddy heat and momentum fluxes further distinguish the dominant mechanisms of SPV influence, pointing to a greater role for direct

https://doi.org/10.5194/egusphere-2026-6696
Preprint. Discussion started: 4 November 2026
© Author(s) 2026. CC BY 4.0 License.

momentum-flux forcing in the polar region in node 12, compared with a stronger contribution from polar heat fluxes in nodes 6 and 9. Together, these diagnostics provide a comprehensive picture of the distinct dynamical characteristics of the identified nodes.

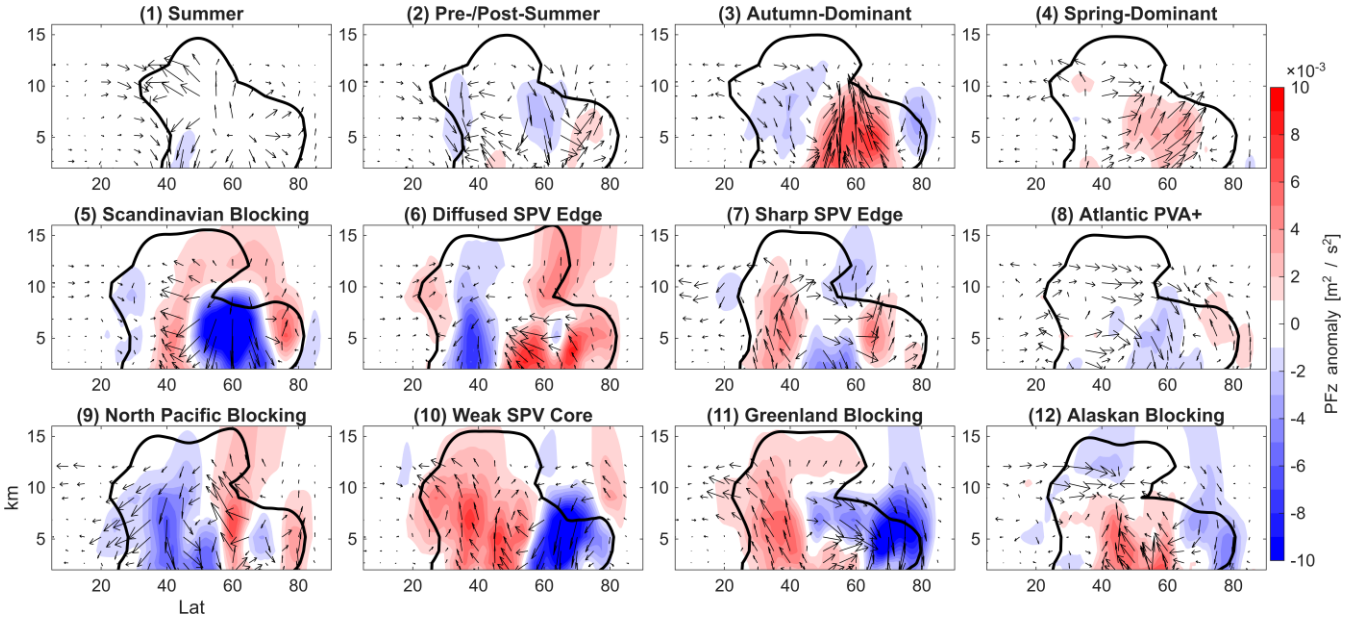


Figure 10: Meridional-vertical cross-sections of the vertical wave activity flux (shading) and meridional-vertical components (vectors) anomalies from monthly gridded climatology. Nodal-mean vertical fluxes ($\pm 0.01\ m^2/s^2$) are denoted by the black contours. The vertical vector components are multiplied by 50 for visibility.

3.4. Impact on the SPV

To relate the lower-SPV-edge configurations discussed above to the state of the upper SPV, Fig. 11 shows composites of 10-hPa, 60°N zonal-mean zonal-wind climatology and deviations from it, centred on transitions into each SOM node. The composites reveal systematic differences in the upper-SPV state associated with different lower-edge configurations, as well as distinct subsequent evolutions following the transition. The seasonal super-group (nodes 1-4) show high compatibility with the seasonal evolution, resulting with negligible anomalies. Nodes 7, 10, and 11 preferentially occur when the 10-hPa circulation is anomalously weak, showing climatological SPV winds below 20 m/s. Following these transitions, the existing negative wind anomalies generally weaken, indicating a subsequent acceleration of the SPV relative to climatology. Conversely, Nodes 6, 9, and 12 are associated with a relatively strong SPV at the time of transition, with positive 10-hPa wind anomalies subsequently decreasing, indicative of SPV deceleration. These contrasting evolutions suggest that the lower-SPV-edge configuration is associated with a systematic subsequent adjustment of the upper-stratospheric circulation.

The Scandinavian Blocking configuration (Node 5) exhibits a somewhat different evolution. Although the absolute 10-hPa wind speed at the transition is relatively strong (~27 m s^{-1}), the anomaly is close to zero. The transition is followed by a short-

https://doi.org/10.5194/egusphere-2026-6696
Preprint. Discussion started: 4 November 2026
© Author(s) 2026. CC BY 4.0 License.

lived but pronounced deceleration, after which the SPV gradually recovers. Node 8, representing a relatively symmetric lower-
370 SPV edge configuration, occurs with an intermediate 10-hPa circulation (~25 m s^{-1}) and is followed by a gradual reduction in the positive wind anomaly. Together with the enhanced Atlantic storm-track activity associated with this node, this evolution is consistent with an eddy–mean-flow interaction in which enhanced wave forcing contributes to subsequent SPV deceleration. Overall, Fig. 11 indicates a systematic temporal relationship between the lower-SPV edge and the upper-SPV circulation. The pre-transition anomalies suggest that the state of the upper SPV preconditions the lower-edge transitions, while the contrasting
375 post-transition evolutions indicate that the lower-edge state is, in turn, associated with subsequent acceleration or deceleration of the upper SPV. Thus, the results imply a two-way interaction between the lower-SPV edge and the upper SPV.

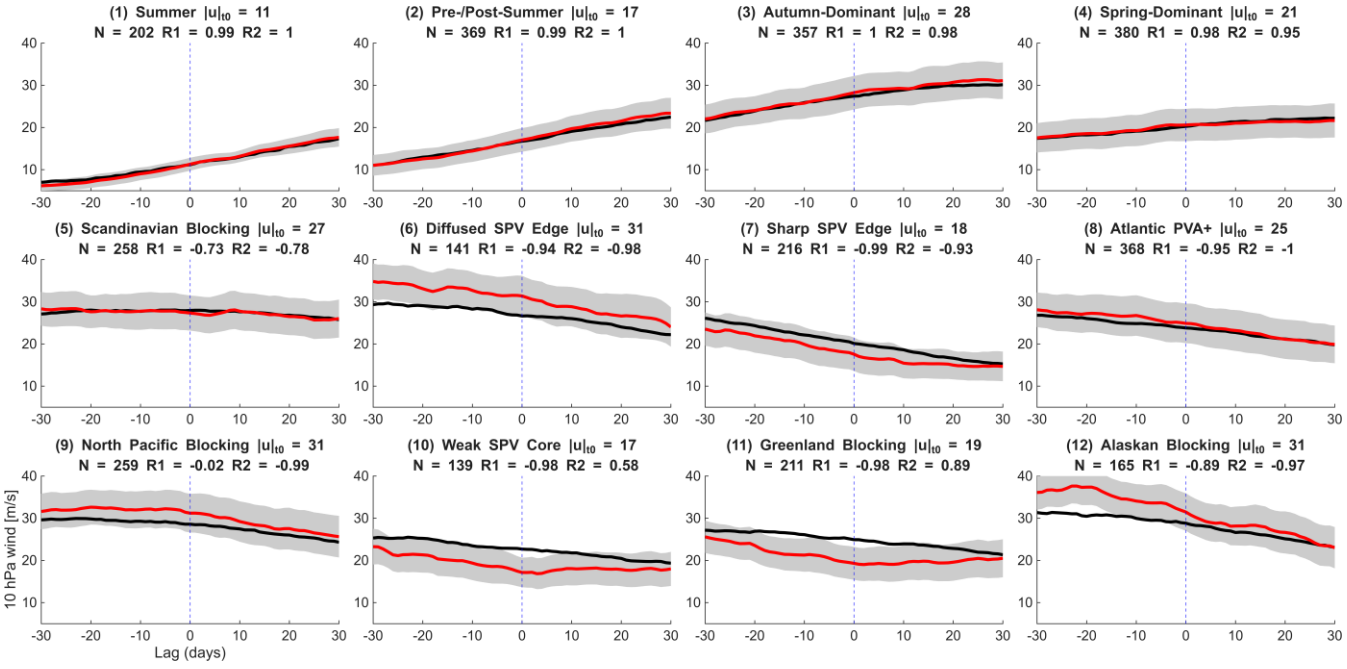


Figure 11: Zonal-mean zonal wind (10hPa, 60N, red lines) and climatology (black lines) composites centred around node entries. Shading denotes the ± 0.25 standard deviation for each time-lag. Titles show Node number and name, followed by the mean 10 hPa
380 **zonal-mean zonal wind speed at t=0, the number of analyzed transitions (N), and the linear correlation coefficient (R) across the 30 days preceding (R1) and following (R2) the transition.**

To further relate the SOM nodes to SSWs, we evaluate anomalous node occupancy around the 29 SSW events detected in the analysis period. These events are defined by the reversal of the zonal-mean zonal winds at the 10 hPa level, in the 60N latitude, occurring strictly within the DJF period. The nodes showing enhanced monthly prior to SSWs are notably the spring-dominant
385 node (4), sharp SPV edge node (7), and the Atlantic PVA+ node (8). The autumn-dominant node (3) is anomalously active during SSWs, while nodes 7 and 11 show enhanced activity in the recovery phase. Despite nodes 6 and 9 leading to the strongest SPV perturbations, these nodes are associated with the stronger initial SPV states and hence show an abnormal

https://doi.org/10.5194/egusphere-2026-6696
Preprint. Discussion started: 4 November 2026
© Author(s) 2026. CC BY 4.0 License.

reduction in frequency around SSWs. As suggested by Davies and Sprenger 2026, the SPV shows reduced stability under an annular mode of enhanced lower-SPV edge, as qualitatively captured by node 7.

Finally, the unusual appearance of the spring-dominant node 4 well within the winter season could potentially serve as a precursor to SSW events, though further analysis is required to establish the predictive potential of this anomaly. Altogether, the lower-SPV edge configurations shed new light on the intricate stratospheric dynamics leading to and following SSW events, emphasizing the role of the lower-SPV edge as a gateway for troposphere-stratosphere coupling.

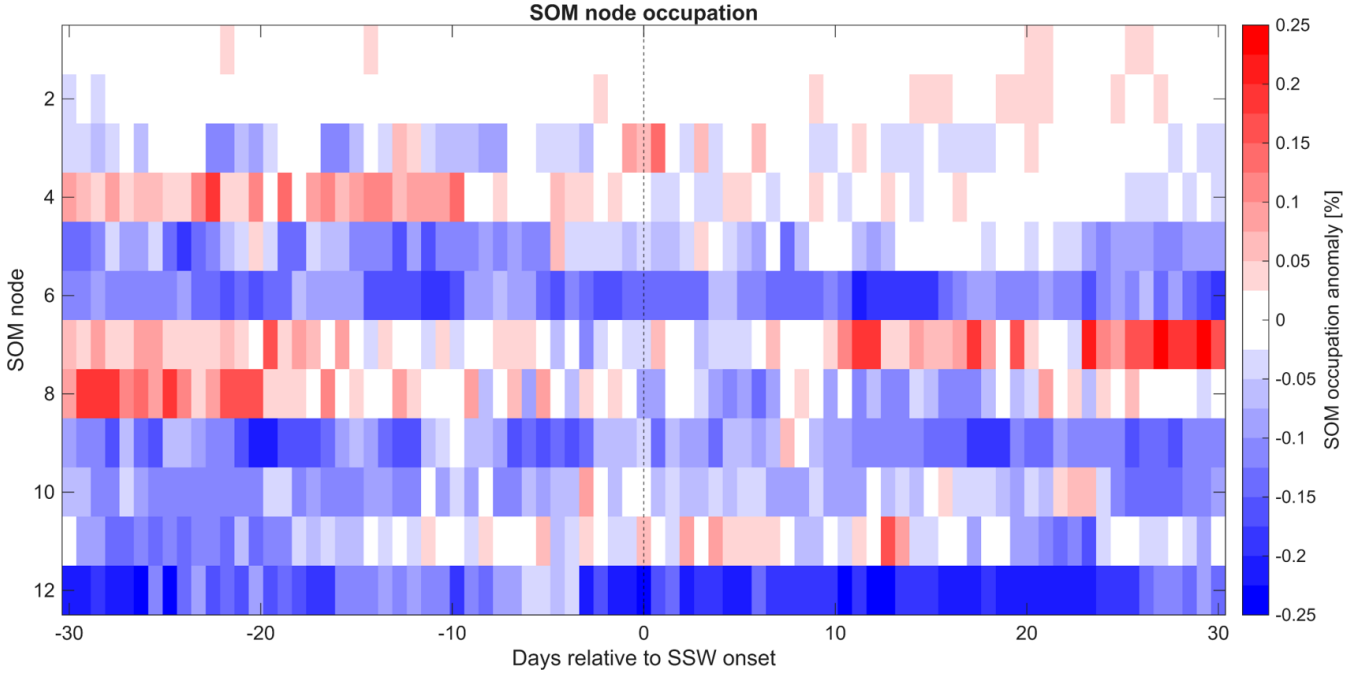


Figure 12: Nodal occupancy anomalies during the 30 days leading to and following SSW events. Shading denotes percent-wise departures from monthly-mean nodal frequencies (see Fig. 2).

4. Summary and discussion

The objectives of this study culminate to enhance our understanding of lower-SPV edge dynamics and predictability. To address these objectives, presented in Section 1, a novel framework for the analysis of SPV-edge configuration archetypes is constructed, resulting with a fundamental characterization of the atmospheric state on global-scale, at daily intervals. The lower SPV has traditionally been characterized using a single potential vorticity contour or SPV-centred diagnostics such as area, centroid location, or strength. While these metrics have proven valuable for describing the large-scale evolution of the vortex, they inherently treat the SPV edge as a morphological boundary rather than as the finite-width dynamical barrier through which troposphere–stratosphere exchange occurs. By explicitly considering the area bounded by the 6 and 7 PVU

https://doi.org/10.5194/egusphere-2026-6696
Preprint. Discussion started: 4 November 2026
© Author(s) 2026. CC BY 4.0 License.

contours on the 350 K isentropic surface, this study demonstrates that the morphology of the SPV edge itself constitutes an additional and dynamically meaningful diagnostic of the lower stratosphere.

The resulting SOM classification reveals that variations in SPV-edge morphology can be decomposed into a limited number of robust, recurrent circulation regimes. These regimes exhibit distinct signatures in terms of vortex strength, edge sharpness, and atmospheric blocking patterns, as well as downward and upward coupling and surface impacts. Particularly noteworthy is that the width of the SPV edge emerges as one of the principal dimensions along which the SOM nodes are separated, indicating that it represents a fundamental characteristic of the lower vortex state.

The association between specific edge morphologies and preferred blocking configurations further highlights the dynamical relevance of the proposed classification. Greenland, Scandinavian, North Pacific, and Alaskan blocking patterns are consistently associated with distinct SPV-edge structures, suggesting that the location of tropospheric blocking is related to how the vortex boundary is shaped and deformed. The results show that different blocking regimes are associated with distinct morphological signatures of the SPV edge, providing a means of characterizing their differing dynamical relationships with the stratospheric vortex.

An equally important result is that the classified regimes exhibit considerable persistence and evolve through a limited number of statistically preferred transition pathways. Although neighbouring SOM nodes represent similar vortex configurations in phase space, transitions frequently bypass these adjacent states in favour of more specific pathways, highlighting that the evolution of the lower-SPV edge is constrained by the underlying dynamics rather than by arbitrary movement across the SOM. Together, these findings suggest that changes in the lower vortex edge are better interpreted as transitions between preferred dynamical states than as unconstrained fluctuations of a continuously varying system.

From a broader perspective, the classification provides a new framework for studying stratosphere–troposphere coupling. Since the lower-SPV edge represents the interface between the isolated polar air mass and the surrounding troposphere, its morphology directly reflects the efficiency of dynamical isolation or mixing. Diagnostics based solely on a single PV contour cannot distinguish between vortices with similar size or position but substantially different edge sharpness and dynamic characteristics. Incorporating the finite-width SPV edge therefore offers a richer description of the lower vortex state and may help explain differences in subsequent vortex evolution and surface impacts among otherwise similar circulation patterns. E.g., despite similar seasonal amplitudes, nodes 6 and 7 portray contrasting SPV-edge widths, associated with contrasting anomalous patterns of surface temperature and pressure anomalies, wave propagation, eddy flux anomalies, and associated SPV response.

Several limitations should nevertheless be acknowledged. The classification is based on climatological reanalysis data and therefore reflects the dominant modes of variability over the analyzed period. Different reanalysis products, pressure levels,

https://doi.org/10.5194/egusphere-2026-6696
Preprint. Discussion started: 4 November 2026
© Author(s) 2026. CC BY 4.0 License.

or PV thresholds may modify the resulting SOM topology, although the physical interpretation is expected to remain robust given the stability of the identified blocking regimes and transition pathways.

Overall, this study demonstrates that treating the lower-SPV edge as a finite-width dynamical feature rather than as a single contour reveals a set of recurrent morphological states with clear physical significance. The proposed classification bridges the morphological description of the polar vortex with its role as a dynamical barrier, providing a physically interpretable framework for investigating vortex variability, regime transitions, and troposphere–stratosphere coupling.

Appendix A – a single PV contour classification and correspondence to maximum PV gradient band

Prior to establishing the double PV contour classification approach, preliminary analysis included using a similar single PV-contour classification, focusing on the 6 PVU contour on the 350 K isentropic surface. The 6 PVU and PV anomaly composites resulting from the single PV contour analysis are shown in Fig. A1. While the nodes do provide a useful separation between different Rossby wavenumbers and phases, meaningful PV anomalies are only centred around the analyzed contour, and no annular modes emerge. We further analyse the dominant wavelength associated to each node, co-occurring surface temperature anomalies, and long-term occurrence trends (not shown). We find that the single-contour approach falls short of capturing non-linear RWB signals in the node composites, and unable to capture the role of the lower-SPV edge as a dynamical barrier as is reflected from the finite-width PV-band approach. The comparison between the PV anomalies projected by the single contour (shading in Fig. A1) and the double contour approach (shading in Fig. 1) clarifies the added values of the latter. This pre-analysis helped consolidate the finite-width PV-band approach as a more appropriate – and influential – diagnostic of the lower-SPV edge.

https://doi.org/10.5194/egusphere-2026-6696
Preprint. Discussion started: 4 November 2026
© Author(s) 2026. CC BY 4.0 License.

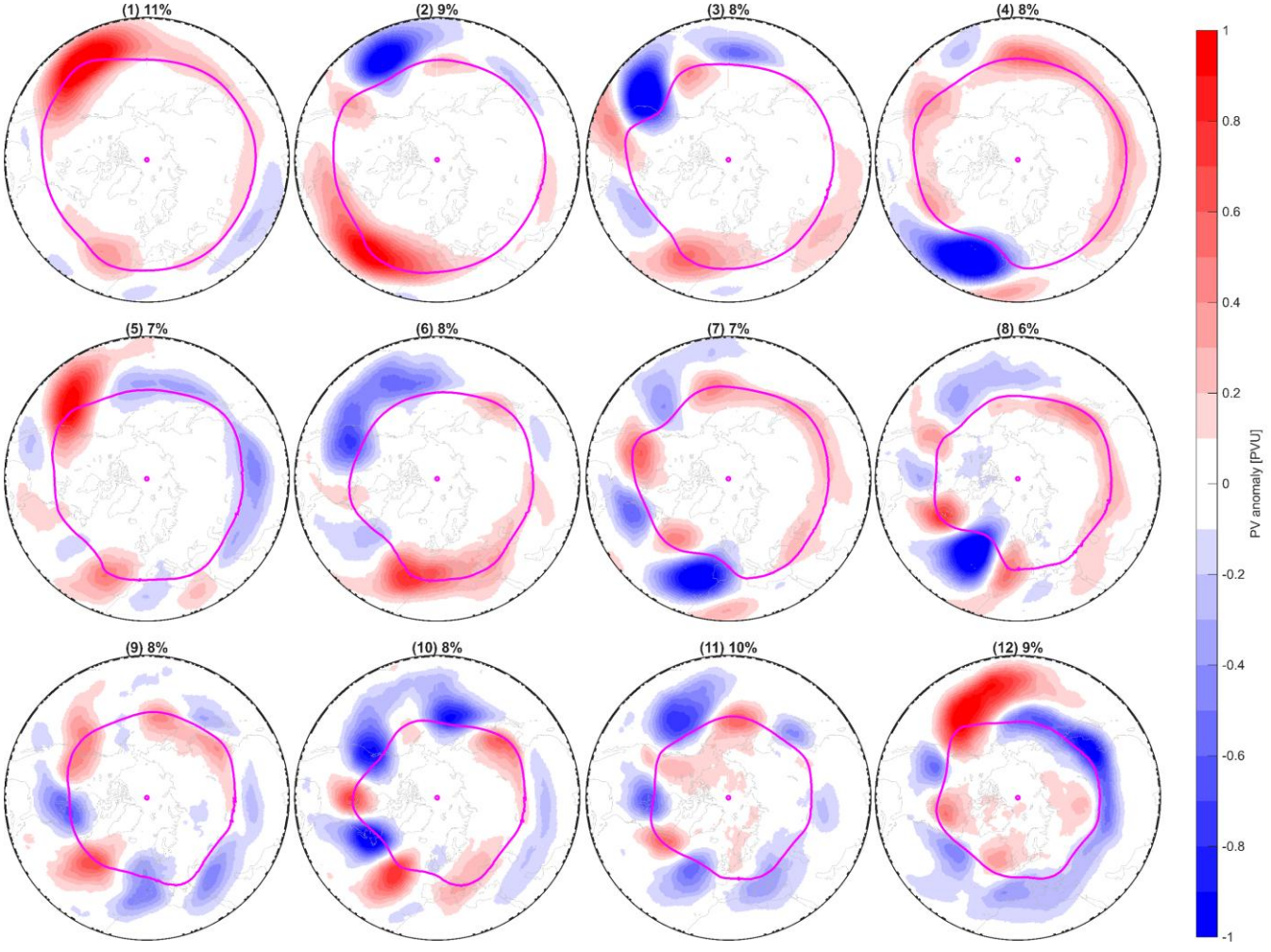


Figure A1. Isentropic PV anomaly and 6 PVU contour composites on the 350K surface from the single PV contour approach. Note that these are different classification results, despite also being separated into 12 groups. Titles denote node number and annual-mean frequency (%).

To further justify the choice of the 6-7 PV band framework, Fig. B1 shows the maximum PV gradient node composites. The maximum PV gradient composite is smoothed using a one-dimensional Gaussian filter with a standard deviation of one grid point, with no constraint to maximum winds. The maximum PV gradient overlaps nicely with the area between the 6-7 PVU contours, suggesting this interval well captures the maximum PV gradients on the corresponding isentropic surface. Surprisingly, the maximum PV gradient composites are only weakly affected by the PV-band configuration, suggesting that the raw maximum PV gradient does not meaningfully reflect the lower-SPV variability. Instead, the maximum PV gradient shows strong geographic dependency, apparently sensitive to land-sea contrast and orographic features.

https://doi.org/10.5194/egusphere-2026-6696
Preprint. Discussion started: 4 November 2026
© Author(s) 2026. CC BY 4.0 License.

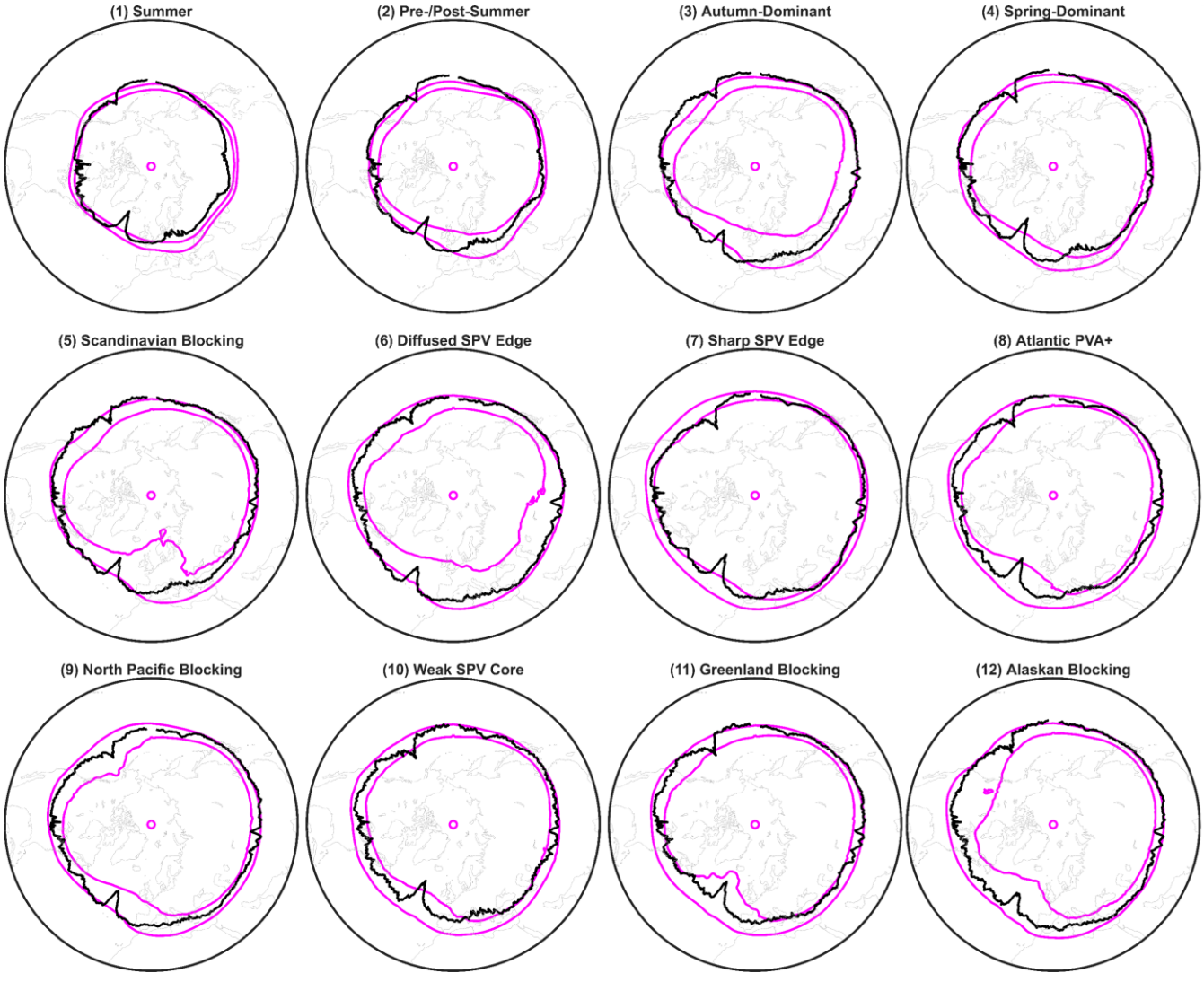


Figure A2. Nodal composites of the maximum PV gradient latitude (black contours), demonstrating the correspondence of the 6-7 PV band (magenta contours) and the maximum PV gradient on the 350K surface. The magenta contours are as in Figure 1.

Code and data availability

The ERA-5 PV data on the 350 K isentropic surface and the code used in the analysis, including the SOM node indices for the analysis period, are available upon request. Other ERA-5 variables are available for direct download on Climate Data Store by Copernicus: ERA5 hourly data on single levels from 1940 to present (last access: 28 September 2026).

https://doi.org/10.5194/egusphere-2026-6696
Preprint. Discussion started: 4 November 2026
© Author(s) 2026. CC BY 4.0 License.

Author contributions

YG and RJW conceptualized the research. YG conducted the research, performed the analysis, and wrote the underlying codes and the manuscript. JW conducted the preliminary single PV contour classification, supervised by YG and RJW. All coauthors took part in reviewing and editing the final draft.

Competing interests

The authors declare that they have no competing interests.

Disclaimer

Copernicus Publications remains neutral with regard to jurisdictional claims made in the text, published maps, institutional affiliations, or any other geographical representation in this paper. While Copernicus Publications makes every effort to include appropriate place names, the final responsibility lies with the authors. Views expressed in the text are those of the authors and do not necessarily reflect the views of the publisher.

Acknowledgements

The authors would like to acknowledge Michael Sprenger of ETH Zurich Institute of Atmosphere and Climate for providing access to post-processed ECMWF ERA-5 isentropic PV data.

Financial support

R.C.J.W. and Y.G. were supported by the Swiss National Science Foundation (Grant PCEFP2-20337).

https://doi.org/10.5194/egusphere-2026-6696
Preprint. Discussion started: 4 November 2026
© Author(s) 2026. CC BY 4.0 License.

References

Afargan-Gerstman, H., Domeisen, D.I.V.: Winter stratospheric extreme events impact European storm damage. *Commun Earth Environ* **6**, 529. https://doi.org/10.1038/s43247-025-02431-w, 2025.

Albers, J. R., and Birner, T.: Vortex preconditioning due to planetary and gravity waves prior to sudden stratospheric warmings. *Journal of the Atmospheric Sciences*, *71*(11), 4028-4054. https://doi.org/10.1175/JAS-D-14-0026.1, 2014.

Antokhina, O.Y., Gochakov, A.V., Zorkaltseva, O.S. *et al.*: Rossby Wave Breaking in the Stratosphere: Part I—Climatology and Long-Term Variability. *Atmos Ocean Opt* **37**, 514–521. https://doi.org/10.1134/S1024856024700696, 2024.

Ayarzagüena, B., Charlton-Perez, A. J., Butler, A. H., Hitchcock, P., Simpson, I. R., Polvani, L. M., et al. : Uncertainty in the response of sudden stratospheric warmings and stratosphere-troposphere coupling to quadrupled CO_2 concentrations in CMIP6 models. *Journal of Geophysical Research: Atmospheres*, 125, e2019JD032345. https://doi.org/10.1029/2019JD032345, 2020.

Bancala, S., Krüger, K., and Giorgetta, M.: The preconditioning of major sudden stratospheric warmings. *Journal of Geophysical Research: Atmospheres*, 117(D4). https://doi.org/10.1029/2011JD016769, 2012.

Baldwin, M. P., and Holton, J. R.: Climatology of the Stratospheric Polar Vortex and Planetary Wave Breaking. *Journal of Atmospheric Sciences*, *45*(7), 1123-1142. https://doi.org/10.1175/1520-0469(1988)045<1123:COTSPV>2.0.CO;2, 1998.

Baldwin, M. P., and Dunkerton, T. J.: Stratospheric harbingers of anomalous weather regimes. *Science*, *294*(5542), 581-584. https://doi.org/10.1126/science.1063315, 2001.

Baldwin, M. P., Ayarzagüena, B., Birner, T., Butchart, N., Butler, A. H., Charlton-Perez, A. J., et al.: Sudden stratospheric warmings. *Reviews of Geophysics*, 59, e2020RG000708. https://doi.org/10.1029/2020RG000708, 2021.

Barnes, E. A., and D. L. Hartmann: Detection of Rossby wave breaking and its response to shifts of the midlatitude jet with climate change, *J. Geophys. Res.*, 117, D09117, doi:10.1029/2012JD017469, 2012.

Barriopedro, D., García-Herrera, R., Lupo, A. R., and Hernández, E.: A Climatology of Northern Hemisphere Blocking. *Journal of Climate*, *19*(6), 1042-1063. https://doi.org/10.1175/JCLI3678.1, 2006.

Berkovic S, Mendelsohn OY, Ilotoviz E, Raveh-Rubin S.: Self-organizing map classification of the boundary layer profile: A refinement of Eastern Mediterranean winter synoptic regimes. *Int J Climatol*. 41: 3317–3338. https://doi.org/10.1002/joc.7021, 2021.

Black, R. X., and McDaniel, B. A.: Submonthly Polar Vortex Variability and Stratosphere–Troposphere Coupling in the Arctic. *Journal of Climate*, *22*(22), 5886-5901. https://doi.org/10.1175/2009JCLI2730.1, 2009.

Bowman, K. P.: Large-scale isentropic mixing properties of the Antarctic polar vortex from analyzed winds, *J. Geophys. Res.*, *98*(D12), 23013–23027, doi:10.1029/93JD02599, 1993.

Bukenberger, M., Rüdisühli, S. and Schemm, S.: Jet stream dynamics from a potential vorticity gradient perspective: The method and its application to a kilometre-scale simulation. *Quarterly Journal of the Royal Meteorological Society*, 149(755, 2409–2432. Available from: https://doi.org/10.1002/qj.4513, 2023.

https://doi.org/10.5194/egusphere-2026-6696
Preprint. Discussion started: 4 November 2026
© Author(s) 2026. CC BY 4.0 License.

Butchart, N., and Remsberg, E. E.: The area of the stratospheric polar vortex as a diagnostic for tracer transport on an isentropic surface. *Journal of Atmospheric Sciences*, *43*(13),1319-1339. https://doi.org/10.1175/1520-0469(1986)043%3C1319:TAOTSP%3E2.0.CO;2, 1986.

Butchart, N.: *The Brewer-Dobson circulation*, *Rev. Geophys.*, 52, doi:10.1002/2013RG000448, 2014.

Charney, J. G., and P. G. Drazin: Propagation of planetary-scale disturbances from the lower into the upper atmosphere, *J. Geophys. Res.*, 66(1), 83–109, doi:10.1029/JZ066i001p00083, 1961.

Cohen, S., Pincus, R. and Polvani, L.M.: Stratospheric cooling and amplification of radiative forcing with rising carbon dioxide. *Nat. Geosci.* **19**, 507–512. https://doi.org/10.1038/s41561-026-01965-8, 2026.

Davies, H. C., and Rossa, A. M.: PV Frontogenesis and Upper-Tropospheric Fronts. *Monthly Weather Review*, *126*(6), 1528-1539. https://doi.org/10.1175/1520-0493(1998)126<1528:PFAUTF>2.0.CO;2, 1998.

Davies, H. C. and Sprenger, M. A.: Transient flow patterns of an annular-like stratospheric polar vortex, Weather Clim. Dynam., 7, 717–741. https://doi.org/10.5194/wcd-7-717-2026, 2026.

Domeisen, D.I.V., Butler, A.H.: Stratospheric drivers of extreme events at the Earth's surface. *Commun Earth Environ* **1**, 59. https://doi.org/10.1038/s43247-020-00060-z, 2020.

Dunn-Sigouin, E., Son, S., and Lin, H.,: Evaluation of Northern Hemisphere Blocking Climatology in the Global Environment Multiscale Model. *Mon. Wea. Rev.*, **141**, 707–727, https://doi.org/10.1175/MWR-D-12-00134.1, 2013.

Garfinkel, C. I., Hartmann, D. L., and Sassi, F.: Tropospheric Precursors of Anomalous Northern Hemisphere Stratospheric Polar Vortices. *Journal of Climate*, *23*(12), 3282-3299. https://doi.org/10.1175/2010JCLI3010.1, 2010.

Garfinkel, C. I., and Waugh, D. W.: Tropospheric Rossby Wave Breaking and Variability of the Latitude of the Eddy-Driven Jet. *Journal of Climate*, *27*(18), 7069-7085. https://doi.org/10.1175/JCLI-D-14-00081.1, 2014.

Givon, Y., Keller Jr., D., Silverman, V., Pennel, R., Drobinski, P., and Raveh-Rubin, S.: Large-scale drivers of the mistral wind: link to Rossby wave life cycles and seasonal variability. *Weather Clim. Dynam.*, *2*, 609–630. https://doi.org/10.5194/wcd-2-609-2021, 2021.

Givon, Y., Hess, O., Flaounas, E., Catto, J. L., Sprenger, M., and Raveh-Rubin, S.: Process-based classification of Mediterranean cyclones using potential vorticity. *Weather Clim. Dynam., 5*, 133–162. https://doi.org/10.5194/wcd-5-133-2024, 2024.

Givon, Y., Keller Jr., D., Drobinski, P., and Raveh-Rubin, S.: Contrasting impact of different Mediterranean cyclones on the hydrological cycle and ocean heat content. *Weather Clim. Dynam., 7*, 567–582. https://doi.org/10.5194/wcd-7-567-2026, 2026.

Gray, L.J., Brown, M.J., Knight, J. *et al.*: Forecasting extreme stratospheric polar vortex events. *Nat Commun* **11**, 4630. https://doi.org/10.1038/s41467-020-18299-7, 2020.

Hall, R. J., Mitchell, D. M., Seviour, W. J. M., and Wright, C. J.: Tracking the stratosphere-to-surface impact of Sudden Stratospheric Warmings. *Journal of Geophysical Research: Atmospheres*, 126, e2020JD033881. https://doi.org/10.1029/2020JD033881, 2021a.

https://doi.org/10.5194/egusphere-2026-6696
Preprint. Discussion started: 4 November 2026
© Author(s) 2026. CC BY 4.0 License.

Hall, R. J., Mitchell, D. M., Seviour, W. J. M., and Wright, C. J.: Persistent model biases in the CMIP6 representation of stratospheric polar vortex variability. *Journal of Geophysical Research: Atmospheres*, 126, e2021JD034759. https://doi.org/10.1029/2021JD034759, 2021b.

Hanna, E., Francis, J., Wang, M., Overland, J. E., Cohen, J., Luo, D., ... and Skific, N.: Influence of high-latitude blocking and the northern stratospheric polar vortex on cold-air outbreaks under Arctic amplification of global warming. *Environmental Research: Climate*, *3*(4), 042004. https://doi.org/10.1088/2752-5295/ad93f3, 2024.

Hannachi, A., Lechner, M., Finke, K. *et al.*: Stratospheric polar vortex, wave absorption/reflection and effect on surface climate. *Clim Dyn 63*, 126. https://doi.org/10.1007/s00382-025-07610-1, 2025.

Haynes, P. H. , McIntyre, M. E. , Shepherd, T. G. , Marks, C. J. , and Shine, K. P.: On the "Downward Control" of Extratropical Diabatic Circulations by Eddy-Induced Mean Zonal Forces. *Journal of Atmospheric Sciences*, *48*(4), 651-678. https://doi.org/10.1175/1520-0469(1991)048<0651:OTCOED>2.0.CO;2, 1991.

Haynes, P., and E. Shuckburgh: Effective diffusivity as a diagnostic of atmospheric transport: 2. Troposphere and lower stratosphere, *J. Geophys. Res.*, 105(D18), 22795–22810, doi:10.1029/2000JD900092, 2000.

Hersbach, H., Bell, B., Berrisford, P., Hirahara, S., Horányi, A., Muñoz-Sabater, J., Nicolas, J., Peubey, C., Radu, R., Schepers, D., Simmons, A., Soci, C., Abdalla, S., Abellan, X., Balsamo, G., Bechtold, P., Biavati, G., Bidlot, J., Bonavita, M., De Chiara, G., Dahlgren, P., Dee, D., Diamantakis, M., Dragani, R., Flemming, J., Forbes, R., Fuentes, M., Geer, A., Haimberger, L., Healy, S., Hogan, R., J., Hólm, E., Janisková, M., Keeley, S., Laloyaux, P., Lopez, P., Lupu, C., Radnoti, G., Rosnay, P., Rozum, I., Vamborg, F., Villaume, S., and Thépaut, L. N.: The ERA5 global reanalysis, Q. J. R. Meteorol. Soc., 146, 1999–2049, https://doi.org/10.1002/qj.3803, 2020.

Hewitson, B. C., and Crane, R. G.: Self-organizing maps: applications to synoptic climatology. *Climate Research*, *22*(1), 13-26. https://doi.org/10.3354/cr022013, 2022.

Holton, J. R., P. H. Haynes, M. E. McIntyre, A. R. Douglass, R. B. Rood, and L. Pfister: Stratosphere-troposphere exchange, *Rev. Geophys.*, *33*(4), 403–439, doi:10.1029/95RG02097, 1995.

IPCC: Climate Change 2021: The Physical Science Basis. Contribution of Working Group I to the Sixth Assessment Report of the Intergovernmental Panel on Climate Change Masson-Delmotte, Zhai, V., P., Pirani, A., Connors, S. L., Péan, C., Berger, S., Caud, N., Chen, Y., Goldfarb ,L., Gomis, M.I., Huang, M., Leitzell, K., Lonnoy, E., Matthews, J. B. R., Maycock, T.K., Waterfield, T., Yelekçi, O., Yu, R., and Zhou B. *Cambridge University Press*, Cambridge, United Kingdom and New York, NY, USA, 2391 pp. https://doi.org/10.1017/9781009157896, 2021.

Karpechko, A. Y., Charlton-Perez, A., Balmaseda, M., Tyrrell, N., and Vitart, F.: *Predicting sudden stratospheric warming 2018 and its climate impacts with a multimodel ensemble*. *Geophysical Research Letters*, 45, 13,538–13,546. https://doi.org/10.1029/2018GL081091, 2018.

Kolstad, E.W., Breiteig, T. and Scaife, A.A.: The association between stratospheric weak polar vortex events and cold air outbreaks in the Northern Hemisphere. Q.J.R. Meteorol. Soc., 136: 886-893. https://doi.org/10.1002/qj.620, 2010.

Kohonen, T.: The self-organizing map. *Proceedings of the IEEE*, *78*(9), 1464-1480. https://doi.org/10.1109/5.58325, 1990.

https://doi.org/10.5194/egusphere-2026-6696
Preprint. Discussion started: 4 November 2026
© Author(s) 2026. CC BY 4.0 License.

Kidston, J., Scaife, A., Hardiman, S. *et al. :* Stratospheric influence on tropospheric jet streams, storm tracks and surface weather. *Nature Geosci* **8**, 433–440. https://doi.org/10.1038/ngeo2424, 2015.

Kunz, A., P. Konopka, R. Müller, and Pan L. L.: *Dynamical tropopause based on isentropic potential vorticity gradients*, *J. Geophys. Res.*, 116, D01110, doi:10.1029/2010JD014343, 2011.

Kunz, A., M. Sprenger, and H. Wernli: *Climatology of potential vorticity streamers and associated isentropic transport pathways across PV gradient barriers*. *J. Geophys. Res. Atmos.*, 120, 3802–3821. doi: 10.1002/2014JD022615, 2015.

Lawrence, Z. D., and Manney, G. L.: Characterizing stratospheric polar vortex variability with computer vision techniques. *Journal of Geophysical Research: Atmospheres*, 123, 1510–1535. https://doi.org/10.1002/2017JD027556, 2018.

Lee, S. H., Furtado, J. C., and Charlton-Perez, A. J.: Wintertime North American weather regimes and the Arctic stratospheric polar vortex. *Geophysical Research Letters*, 46, 14892–14900. https://doi.org/10.1029/2019GL085592, 2019.

Lin, J. and Emanuel, K.: Why the lower stratosphere cools when the troposphere warms, Proc. Natl. Acad. Sci. U.S.A. 121 (11) e2319228121, https://doi.org/10.1073/pnas.2319228121, 2024.

Martius, O., L. M. Polvani, and Davis H. C.: Blocking precursors to stratospheric sudden warming events, *Geophys. Res. Lett.*, 36, L14806, doi:10.1029/2009GL038776, 2009.

McIntyre, M. E.: How well do we understand the dynamics of stratospheric warmings? *Journal of the Meteorological Society of Japan. Ser. II*, **60**(1), 37–65. https://doi.org/10.2151/jmsj1965.60.1_37, 1982.

McIntyre, M. E., and Palmer, T. N.: Breaking planetary waves in the stratosphere. *Nature*, **305**, 593–600. https://doi.org/10.1038/305593a0, 1983.

Mitchell, D. M., Charlton-Perez, A. J., and Gray, L. J.: Characterizing the variability and extremes of the stratospheric polar vortices using 2D moment analysis. *Journal of the Atmospheric Sciences*, *68*(6), 1194-1213. https://doi.org/10.1175/2010JAS3555.1, 2011.

Mitchell, D. M., Osprey, S. M., Gray, L. J., Butchart, N., Hardiman, S. C., Charlton-Perez, A. J., and Watson, P.: The Effect of Climate Change on the Variability of the Northern Hemisphere Stratospheric Polar Vortex. *Journal of the Atmospheric Sciences*, *69*(8), 2608-2618. https://doi.org/10.1175/JAS-D-12-021.1, 2012.

Mizuta, R., and Yoden, S.: Chaotic Mixing and Transport Barriers in an Idealized Stratospheric Polar Vortex. *Journal of the Atmospheric Sciences*, *58*(17), 2616-2629. https://doi.org/10.1175/1520-0469(2001)058<2616:CMATBI>2.0.CO;2, 2001.

Nash, E. R., P. A. Newman, J. E. Rosenfield, and M. R. Schoeberl: An objective determination of the polar vortex using Ertel's potential vorticity, *J. Geophys. Res.*, 101(D5), 9471–9478. 10.1029/96JD00066, 1996.

Neu, J. L., L. C. Sparling, and R. A. Plumb: Variability of the subtropical “edges” in the stratosphere, *J. Geophys. Res.*, 108, 4482, doi:10.1029/2002JD002706, 2003.

Plumb, R. A.: Three-Dimensional Propagation of Transient Quasi-Geostrophic Eddies and Its Relationship with the Eddy Forcing of the Time—Mean Flow. *Journal of Atmospheric Sciences*, *43*(16), 1657-1678. https://doi.org/10.1175/1520-0469(1986)043<1657:TDPOTQ>2.0.CO;2, 1986.

https://doi.org/10.5194/egusphere-2026-6696
Preprint. Discussion started: 4 November 2026
© Author(s) 2026. CC BY 4.0 License.

Rao, J., Garfinkel, C. I., and White, I. P.: Predicting the downward and surface influence of the February 2018 and January 2019 sudden stratospheric warming events in subseasonal to seasonal (S2S) models. *Journal of Geophysical Research: Atmospheres*, 125, e2019JD031919. https://doi.org/10.1029/2019JD031919, 2020.

Rypina, I. I., Brown, M. G., Beron-Vera, F. J., Koçak, H., Olascoaga, M. J., and Udovydchenkov, I. A.: On the Lagrangian Dynamics of Atmospheric Zonal Jets and the Permeability of the Stratospheric Polar Vortex. *Journal of the Atmospheric Sciences*, *64*(10), 3595-3610. https://doi.org/10.1175/JAS4036.1, 2007.

Santee, M. L., Manney, G. L., Livesey, N. J., Froidevaux, L., Schwartz, M. J., & Read, W. G.: Trace gas evolution in the lowermost stratosphere from Aura Microwave Limb Sounder measurements. *Journal of Geophysical Research: Atmospheres*, *116*(D18). https://doi.org/10.1029/2011JD015590, 2011.

Schoeberl M. R. and Hartmann D. L.: The Dynamics of the Stratospheric Polar Vortex and Its Relation to Springtime Ozone Depletions. *Science 251*, 46-52. https://doi.org/10.1126/science.251.4989.46, 1991.

Seviour, W. J. M.: Weakening and shift of the Arctic stratospheric polar vortex: Internal variability or forced response?. *Geophys. Res. Lett.*, *44*, 3365–3373, doi:10.1002/2017GL073071, 2017.

Serra, M., Sathe, P., Beron-Vera, F., and Haller, G.: Uncovering the Edge of the Polar Vortex. *Journal of the Atmospheric Sciences*, *74*(11), 3871-3885. https://doi.org/10.1175/JAS-D-17-0052.1, 2017.

Serreze M. C., and Barry R. G.: Processes and impacts of Arctic amplification: A research synthesis, *Global and Planetary Change*, *77*(1–2), 85-96, https://doi.org/10.1016/j.gloplacha.2011.03.004, 2011.

Sheridan, S. C., and Lee, C. C.: The self-organizing map in synoptic climatological research. *Progress in Physical Geography*, *35*(1), 109-119. https://doi.org/10.1177/0309133310397582, 2011.

Sprenger, M., Wernli, H., and Bourqui, M.: Stratosphere–Troposphere Exchange and Its Relation to Potential Vorticity Streamers and Cutoffs near the Extratropical Tropopause. *Journal of the Atmospheric Sciences*, *64*(5), 1587-1602. https://doi.org/10.1175/JAS3911.1, 2007.

Tibaldi, S., and Molteni, F.: Atmospheric Blocking in Observation and Models. *Oxford Research Encyclopedia of Climate Science* (New York, NY, online edition, Oxford Academic). https://doi.org/10.1093/acrefore/9780190228620.013.611, 2018.

Thompson, D. W. J., M. P. Baldwin, and J. M. Wallace: Stratospheric Connection to Northern Hemisphere Wintertime Weather: Implications for Prediction. *J. Climate*, *15*, 1421–1428, https://doi.org/10.1175/1520-0442(2002)015<1421:SCTNHW>2.0.CO;2, 2002.

Turhal, K., Plöger, F., Clemens, J., Birner, T., Weyland, F., Konopka, P., and Hoor, P.: Variability and trends in the potential vorticity (PV)-gradient dynamical tropopause, *Atmos. Chem. Phys.*, *24*, 13653–13679. https://doi.org/10.5194/acp-24-13653-2024, 2024.

Tyrlis, E., and Hoskins B. J.: Aspects of a Northern Hemisphere Atmospheric Blocking Climatology. *J. Atmos. Sci.*, **65**, 1638–1652, https://doi.org/10.1175/2007JAS2337.1, 2008.

https://doi.org/10.5194/egusphere-2026-6696
Preprint. Discussion started: 4 November 2026
© Author(s) 2026. CC BY 4.0 License.

Wang, N., Biggs, T. W., and Skupin, A.: Visualizing gridded time series data with self organizing maps: An application to multi-year snow dynamics in the Northern Hemisphere. *Computers, environment and urban systems*, *39*, 107-120. https://doi.org/10.1016/j.compenvurbsys.2012.10.005 2013.

Waugh, D. W., Sobel, A. H., and Polvani, L. M.: What Is the Polar Vortex and How Does It Influence Weather?. *Bulletin of the American Meteorological Society*, *98*(1), 37-44. https://doi.org/10.1175/BAMS-D-15-00212.1, 2017.

Wichrowski, L., Pérez-Carrasquilla, J. S., and Molina, M. J.: Weather regime diversity, transitions, and trends using hexagonal self-organizing maps. *Journal of Geophysical Research: Atmospheres*, *131*(8), e2025JD044874. https://doi.org/10.1029/2025JD044874, 2026.

White, I., Garfinkel, C. I., Gerber, E. P., Jucker, M., Aquila, V., and Oman, L. D.: The downward influence of sudden stratospheric warmings: Association with tropospheric precursors. *Journal of Climate*, *32*(1), 85-108. https://doi.org/10.1175/JCLI-D-18-0053.1, 2019.

White, I. P., Garfinkel, C. I., Gerber, E. P., Jucker, M., Hitchcock, P., and Rao, J.: The Generic Nature of the Tropospheric Response to Sudden Stratospheric Warmings. *Journal of Climate*, *33*(13), 5589-5610. https://doi.org/10.1175/JCLI-D-19-0697.1, 2020.

Wu, Y., Simpson, I. R., and Seager, R.: Intermodel spread in the Northern Hemisphere stratospheric polar vortex response to climate change in the CMIP5 models. *Geophysical Research Letters*, 46, 13290–13298. https://doi.org/10.1029/2019GL085545, 2019.

Xia, Y., Xie, F., Luo, F. et al.: Stratospheric polar vortex shapes Arctic surface climate via a radiative pathway. *Nat Commun* **17**, 5996. https://doi.org/10.1038/s41467-026-72698-w, 2026.

Yang, P., Bao, M., Ren, X., and Tan, X.: The role of vortex preconditioning in influencing the occurrence of strong and weak sudden stratospheric warmings in ERA5 reanalysis. *Journal of Climate*, *36*(4), 1197-1212. https://doi.org/10.1175/JCLI-D-22-0319.1, 2023.

Zuev, V.V., Savelieva, E.S. and Pavlinsky, A.V.: Features of Stratospheric Polar Vortex Weakening Prior to Breakdown. *Atmos Ocean Opt* **35**, 183–186. https://doi.org/10.1134/S1024856022020142, 2022.

Zuev, V.V., Savelieva, E.S.: Dynamic Characteristics of the Stratospheric Polar Vortices. *Dokl. Earth Sc.* **517**, 1240–1248. https://doi.org/10.1134/S1028334X24601895, 2024.